2018

Nonlinear Coupled Effects in Nanomaterials

Sia Bhowmick
bhow6290@mylaurier.ca

WILFRID LAURIER UNIVERSITY

MASTERS THESIS

Nonlinear Coupled Effects in Nanomaterials

Author:

Sia Bhowmick

Supervisors:

Dr. Roderick Melnik

Dr. Manuele Santoprete

A thesis submitted in fulfillment of the requirements

for the degree of Master of Science

in

Mathematics

December 15, 2017

Abstract

Materials at the nanoscale have different chemical, structural, and optoelectrical properties compared to their bulk counterparts. As a result, such materials, called nanomaterials, exhibit observable differences in certain physical phenomena. One such resulting phenomenon called the piezoelectric effect has played a crucial role in miniature self-powering electronic devices called nanogenerators which are fabricated by using nanostructures, such as nanowires, nanorods, and nanofilms. These devices are capable of harvesting electrical energy by inducing mechanical strain on the individual nanostructures. Electrical energy created in this manner does not have environmental limitations. In this thesis, important coupled effects, such as the nonlinear piezoelectric effect of a semiconducting wurtzite ZnO nanowire are studied by solving a time-dependent thermo-electro-mechanical model. For the examples considered here, the mathematical model consists of a system of fully-coupled nonlinear partial differential equations, and it is solved by using a variational formulation based on finite element representation. The numerical solution to this model is compared with the results obtained for the linear model of piezoelectric effect. The main focus has been given to the results from finite element analysis as a generalized model of the ZnO nanowire in order to understand its characteristics at an unperturbed state.

Contents

List of Figures

List of Tables

List of Abbreviations

TEM	**t**hermo-**e**lectro-**m**echanical
NW	**n**ano**w**ire
M-S-M	**m**etal-**s**emiconductor-**m**etal
MMS	**m**ethod of **m**anufactuerd **s**olutions
MUMPS	**MU**ltifrontal **M**assively **P**arallel sparse direct **S**olver

Physical Constants

Boltzmann constant	$k_B = 1.380\,648\,52(79) \times 10^{-23}\,\mathrm{J\,K^{-1}}$
Dielectric coefficients / permittivity tensors[1]	$\kappa_{11} = 7.57$
	$\kappa_{33} = 9.03$
Electron lifetime	$\tau_n = 0.1 \times 10^{-6}\,\mathrm{s}$
Electron mobility	$\mu_n = 2000\,\mathrm{cm^2V^{-1}s^{-1}}$
Hole lifetime	$\tau_p = 0.1 \times 10^{-6}\,\mathrm{s}$
Hole mobility	$\mu_p = 20\,\mathrm{cm^2V^{-1}s^{-1}}$
Intrinsic carrier concentration	$n_i = 1 \times 10^{6}\,\mathrm{cm^{-3}}$
Mass density[1]	$\rho = 5.61\,\mathrm{gcm^{-3}}$
Maximum donor doping concentration	$N_{Dn-max} = 1 \times 10^{17}\,\mathrm{cm^{-3}}$
n-type background doping concentration	$N_{Dn} = 1 \times 10^{15}\,\mathrm{cm^{-3}}$
Permittivity of free space	$k_0 = 8.854\,187\,817 \times 10^{-12}\,\mathrm{F\,m^{-1}}$
Piezoelectric strain coefficients[1]	$e_{15} = -0.45\,\mathrm{Cm^{-2}}$
	$e_{31} = -0.61\,\mathrm{Cm^{-2}}$
	$e_{33} = 1.15\,\mathrm{Cm^{-2}}$
	$e_{311} = 3.98\,\mathrm{Cm^{-2}}$
	$e_{313} = 1.21\,\mathrm{Cm^{-2}}$
	$e_{333} = -5.59\,\mathrm{Cm^{-2}}$
Primary pyroelectric coefficients[1]	$\gamma_x = 0\,\mathrm{Cm^{-2}K^{-1}}$
	$\gamma_z = -1.2 \times 10^{-5}\,\mathrm{Cm^{-2}K^{-1}}$

[1] physical constants specific to ZnO nanomaterials

Reference temperature	$T_0 = 300\,\mathrm{K}$
Stiffness coefficients / Elasticity tensors[1]	$C_{11} = 20.97 \times 10^{10}\,\mathrm{Nm^{-2}}$
	$C_{13} = 10.51 \times 10^{10}\,\mathrm{Nm^{-2}}$
	$C_{33} = 21.09 \times 10^{10}\,\mathrm{Nm^{-2}}$
	$C_{55} = 4.247 \times 10^{10}\,\mathrm{Nm^{-2}}$
Spontaneous polarization[1]	$P^{sp}_{piezo} = -0.01\,\mathrm{Cm^{-2}}$
Spreading width of doping concentration	$ch = 4.66 \times 10^{-9}\,\mathrm{m}$
Thermal conductivity[1]	$k_{11} = 18\,\mathrm{Wm^{-1}K^{-1}}$
	$k_{33} = 18\,\mathrm{Wm^{-1}K^{-1}}$
Thermal stress tensor coefficients[1]	$\beta_{11} = 9.9608 \times 10^{5}\,\mathrm{Nm^{-2}K^{-1}}$
	$\beta_{33} = 6.1161 \times 10^{5}\,\mathrm{Nm^{-2}K^{-1}}$
Unit charge of electron	$q = 1.602\,176\,620\,8(98) \times 10^{-19}\,\mathrm{C}$

List of Principal Variables

$\vec{u}$	elastic displacement	m
ϕ	electrostatic potential	V
n	electron concentration	m^{-3}
p	hole concentration	m^{-3}
T	absolute temperature	K
J_n	electron current density	Am^{-2}
J_p	hole current density	Am^{-2}
σ	stress	Nm^{-2}

To my beloved parents...

Chapter 1

Introduction

1.1 Nanomaterials and Why They Are Useful

Nanomaterials are the group of materials where at least one of the dimensions is measured in the 1 nm - 100 nm range. They have been studied extensively because of their unique properties owing to their substantially large surface area to volume ratio. Nanomaterials display different chemical, mechanical, electrical, and optical properties based on their chemical and structural compositions. Because of these range of different properties, nanomaterials have been used in scientific and engineering research and development, from drug delivery in the human body to fabricating novel electronic devices [1], [2].

Some nanomaterials have the ability to convert between mechanical and electrical energy due to the presence of electromechanical coupling in the material [3]. This phenomenon known as the *piezoelectric effect* (see section 1.2) has been used in the form of nanogenerators to harvest clean and renewable energy from abundant mechanical energy sources in the environment [4], [5]. Energy harvesting using nanogenerators involves inducing mechanical strain in nanomaterials to discharge electric current or voltage. Electrical energy created in this manner does not have environmental limitations [5].

1.2 The Origin of Piezoelectric Effect

Piezoelectricity means electricity generated from pressure. The word *piezo* means "pressure", which is derived from the Greek word *piezein* "to press tight, squeeze" [6]. Piezoelectric effect is classified into two categories - *direct* and *converse* (also known as *indirect*). The direct piezoelectric effect is the phenomenon by which electric charge is induced in a material subjected to mechanical stress because of its surface charge separation. It was discovered by Pierre and Jacques Curie in 1880 [7]. The converse piezoelectric effect is the reverse procedure where mechanical strain is induced in the presence of applied electric field. It was first predicted mathematically by Gabriel Lippmann in 1881 from fundamental thermodynamic principles [8] and later proved by the Curie brothers [9]. Piezoelectric materials are thus a type of transducer. The first practical application of piezoelectric devices was SONAR, which was developed by Paul Langevin during the World War I to detect submarines under water [10]. Since then, piezoelectric materials have been used to develop different types of devices, such as transformers [11], sensors [12], actuators [13], motors [14], MEMS (Microelectromechanical systems) devices for electrical [15] and biomedical [16] applications, acoustic devices [17], and energy harvesters [18].

1.3 Characteristics of Piezoelectric Materials

Whether a material is piezoelectric depends on its microscopic charge distribution. Piezoelectric materials are known to exhibit spontaneous polarization

as a result of formation of spontaneous dipole moments. Therefore, piezoelectric materials must be polar and non-centrosymmetric, i.e., there must not be an inversion centre [16], [19]. Dipole moments exist in polar materials because the centres of positive and negative charges are not the same. That is why, due to this charge coupling, piezoelectric materials are classified under the group of materials called *smart materials* [16], [20]. Smart materials themselves have been utilized in numerous energy harvesting applications. Some of the most recent advancements include using electromechanical behaviour of cellulose with ZnO nanocoating to harvest vibrational energy [21] and using a plasticizer-modified electrostrictive polymer for mechanical energy harvesting [22]. When piezoelectric materials are subjected to mechanical stress (in case of the direct piezoelectric effect), the shape of the material changes, disrupting their inherent charge distribution. This generates dipole moments in addition to those generated as a result of spontaneous polarization. Similarly, with converse piezoelectric effect, applying an external electric field to the piezoelectric material alters the natural charge distribution which results in mechanical stress and strain [16], [19].

Piezoelectric materials can be both synthetic and natural, the latter of which include quartz crystals, Rochelle salt, sucrose, and topaz [19]. Synthetic piezoelectric materials are created by heating materials above their Curie temperature and applying electric field to align the dipoles [19], [23].

1.4 Significance of Piezoelectric Nanomaterials and Nanogenerators

Traditionally, piezoelectric ceramic quartz have been used to fabricate devices which are used as power sources, motors, in control applications, and many more [24], [25], [26]. Ever since the piezoelectric effect has been observed in nanomaterials, extensive research has been conducted to investigate novel possibilities owing to their unique properties [4], [15], [27], [28], [29]. Piezoelectric nanomaterials are known to be more flexible and endure higher stress compared to their bulk counterparts [1], [30], [31]. These differences along with the inherent properties of nanomaterials have led to fabrication of novel 1-D nanostructures (such as nanotubes, nanowires, and nanorods) that have overcome limitations of bulk materials [4], [29], [32], [33].

Over the last decade, interest in piezoelectric nanomaterials have increased because of the need to fabricate miniature piezoelectric generators [16], [18], [34]. The term piezoelectric "nanogenerator" was first coined by Wang and Song in 2006 [18], where several millivolts of output voltage was generated by bending a zinc oxide nanowire (ZnO NW) by using an Atomic Force Microscope's (AFM) tip. Piezoelectric nanogenerators, as the name suggests, are miniature devices that are fabricated using 1-D piezoelectric nanostructures. The flexibility of the nanomaterial depends on the choice of substrate used for material growth [4]. There are different types of nanogenerator structures which are chosen based on efficiency and ease of fabrication. The two most common arrangements are Vertical NW Integrated Nanogenerator (VING) arrays and Lateral NW Integrated Nanogenerator

(LING) networks, out of which the VING arrays are the more popular choice as it is easier to synthesize vertical ZnO NW arrays [4].

Nanogenerators can be used to drive low-power micro-/nanodevices or recharge batteries. The motivation behind perfecting nanodevices is to fabricate self-powering devices that can harvest small-scale mechanical energy or wasted energy from the environment [18], [29]. In the long run, these devices will be more cost-effective and efficient compared to the traditional rechargeable batteries. For example, a self-powered pacemaker that operate by utilizing mechanical energy from movements of the body can save patients inconvenient and sometimes life-threatening surgeries that are required to replace the batteries every seven years [35].

1.5 In This Thesis

Until recently, mathematical models describing the piezoelectric effect were constructed by considering only the linear piezoelectric behaviour of the material, where the quadratic terms associated with electrical polarization were ignored [31], [36]. However, recent experimental results showed that accounting for the nonlinear piezoelectric behaviour of the material generated results with opposite signs for polarization on the NW under compressive/tensile strain, compared to the linear model of piezoelectric effect [37], [38]. The nonlinear model of the piezoelectric effect will be the main focus in this thesis. The mathematical model studied here will extend upon the state of the art research by Araneo *et al* [30] that was

published in May 2016. In their research, a physically-based model of the nonlinear direct piezoelectric effect was incorporated into a thermo-electro-mechanical (TEM) system in order to study the steady-state current-voltage characteristics of ZnO NWs under a vertical strain (both compressive and tensile) in one dimension. The mathematical model considered comprised five fully-coupled nonlinear partial differential equations (PDEs). In this thesis, a novel time-dependent TEM model of the NW will be considered in two dimensions. The TEM model will be constructed using a system of fully-coupled partial differential equations (PDEs), and the solution will be numerically approximated using a variational formulation based on finite element representation.

Chapter 2

Mathematical Model

2.1 Background

In this research, the time-dependent TEM model of nanomaterials is used to study the coupled effects focusing on the nonlinear piezoelectric effect. This model is constructed by using the classical continuum approach as it has been known to give a successful description of many nanodevices [31], [39], [40]. The mathematical model used to account for the thermal, electrical, and mechanical couplings is based on the Fourier, Poisson, current continuity, and elasticity equations. These equations are fully coupled through the constitutive equations relating thermal, electrical, and mechanical quantities of the piezoelectric media [31], [36], [39], [41], [42], [43].

The time-dependence in the coupled system is examined with respect to the mechanical and thermal behaviour and the charge distribution in the NW. In piezoelectric materials, the velocity of the elastic waves is much smaller than the velocity of the electromagnetic waves [19]. That is why the electric field generated in piezoelectric materials is assumed to be quasi-static [19]. Therefore, the magnetic field observed as a result of the elastic waves is negligible [19], [41]. A 2-D model in the xz-plane of the Cartesian coordinate system is considered in this thesis, which is a good approximation for the analysis of NWs.

2.2 Physical Setup of a Piezoelectric Nanogenerator

The typical model of the piezoelectric nanogenerator is given by the following metal-semiconductor-metal (M-S-M) structure. This M-S-M structure is a type of heterojunction system, where one material is a piezoelectric semiconductor and the other one is a metal [44].

FIGURE 2.1: Schematic of n-doped ZnO NW transistor

The NW in between the two metal contacts acts as the semiconductor, which is chosen to be n-doped with shallow impurities that readily ionize. This means that the free carrier density is equal to the impurity concentration. ZnO is a popular choice for n-doped semiconducting NWs because of its wide band gap ($\sim 3.4eV$), large bond strength, excellent chemical and thermal stability, ability to withstand large elastic deformation, and low cost [45], [46], [47]. ZnO has also been used to create memristive devices using NWs [48], and in bandstructure calculations of ZnO quasiparticles and pseudopotential description [49], [50].

In the M-S-M structure, the ZnO NW forms Schottky contacts with metals, such as gold, as a result the high work function of metallic gold. Schottky contacts are rectifying contacts which allow electrons to flow from ZnO to gold and not the other way, and thus this M-S-M setup is basically two back-to-back Schottky

diodes [44]. ZnO and gold forms Schottky contacts with high work function. The Schottky barrier height is proportional to the piezoelectric charge density at the M-S junctions and is in turn proportional to the induced strain. As a result, this type of structure has a significant influence on current flow inside the nanogenerator [36], [44]. The c-axis (or, vertical crystallographic axis) of the NW is assumed to be oriented along the z-axis as per convention.

A piezoelectric potential (piezopotential) can be created in such devices when mechanical stress is applied to non-centrosymmetric materials like ZnO (i.e., materials lacking an inversion centre). The most commonly used physical setup of such devices consists in fixing (for example, by means of a silver paste) the two ends of a set of parallel NWs or a single NW on a flexible substrate [36], [51]. When the substrate is bent, assuming that the substrate's radius of curvature is much larger than the NW length, an almost purely tensile/compressive strain is generated on the NW [30].

2.3 System of Strongly Coupled Nonlinear PDEs

The time-dependent TEM system is defined using five fully coupled non-linear PDEs of parabolic, hyperbolic, and elliptic types. Even though the model studied in this thesis is in 2-D, the equations are represented in 3-D for notational simplicity. The governing equations are as follows:

$$\frac{\partial^2 \vec{u}}{\partial t^2} = \frac{1}{\rho}\vec{\nabla} \cdot \underline{\underline{\sigma}}\,, \tag{2.3.1}$$

$$\vec{\nabla} \cdot \vec{D} = q(p - n + N)\,, \tag{2.3.2}$$

$$\frac{\partial n}{\partial t} = \frac{1}{q}\vec{\nabla} \cdot \vec{J}_n + U_n \,, \tag{2.3.3}$$

$$\frac{\partial p}{\partial t} = -\frac{1}{q}\vec{\nabla} \cdot \vec{J}_p + U_p \,, \tag{2.3.4}$$

$$\frac{\partial T}{\partial t} = \frac{1}{C\rho}(\underline{\underline{k}}\nabla^2 T) + \frac{1}{C\rho}Q \,. \tag{2.3.5}$$

In the elasticity equation (2.3.1), which is of hyperbolic type, $\vec{u}$ represents the elastic displacement dependent on the spatial coordinates, $\underline{\underline{\sigma}}$ is the Cauchy stress tensor, and ρ is the material density.

The Poisson (2.3.2) and the current continuity equations (2.3.3 and 2.3.4) play a fundamental role in semiconductor device modelling. The Poisson equation formulates a relationship between the electrostatic potential ϕ and the charge distribution. Here, $\vec{D}$ is dielectric displacement vector, q is the electric charge, p and n are the hole and electron carrier concentrations, and N is the net doping concentrations of ionized donors and acceptors.

The current continuity equations are derived using Ampere's law [52], [53]:

$$\vec{\nabla} \times \vec{H} = \frac{\partial \vec{D}}{\partial t} + \vec{J} \,. \tag{2.3.6}$$

By applying the divergence operator on this equation and splitting the conduction current density $\vec{J}$ into $\vec{J}_n$ and $\vec{J}_p$, for electrons and holes respectively, and by assuming that all charges in the semiconductors, except the mobile carriers (electrons and holes), are time invariant, the following current continuity equation is obtained [52]:

$$\vec{\nabla} \cdot (\vec{J_n} + \vec{J_p}) + q\frac{\partial}{\partial t}(p - n) = 0\,. \tag{2.3.7}$$

In order to interpret this equation easily, it is split into the forms given by equations (2.3.3) and (2.3.4) by introducing the quantities U_n and U_p, which describes the net generation (G) - recombination (R) rates of electrons and holes, respectively ($U_n = U_p = G - R$). The generation rates in this model are assumed to be zero as there are no external light sources present in the main examples considered here. However, the model can be extended to this case too. The recombination rates of electrons and holes are defined through a trap-assisted mechanism, which is given by the Schokley-Read-Hall formula [53], [54]:

$$R = \frac{pn - n_i^2}{\tau_p(n + n_t) + \tau_n(p + p_t)}\,. \tag{2.3.8}$$

Therefore,

$$U_n = U_p = \frac{n_i^2 - pn}{\tau_p(n + n_t) + \tau_n(p + p_t)}\,. \tag{2.3.9}$$

where τ_n and τ_p are electron and hole carrier lifetimes, and n_t and p_t are electron and hole trap densities. The quantities n_t and p_t can be assumed to be equal to the intrinsic carrier concentration n_i [30].

In semiconductors, current flow occurs because of two major effects - the drift of charge carriers due to the influence of an electric current and the diffusion current due to the concentration gradient of the charge carriers. These drift and diffusion components can be combined into the following equations for electron and hole current densities:

$$\vec{J_n} = qn\mu_n\vec{E} + qD_n\vec{\nabla}n\,, \tag{2.3.10}$$

$$\vec{J_p} = qp\mu_p\vec{E} - qD_p\vec{\nabla}p\,, \tag{2.3.11}$$

where μ_n and μ_p denote the electron and hole mobilities, and $D_n = \mu_n\frac{k_BT}{q}$ and $D_p = \mu_p\frac{k_BT}{q}$ denote the Einstein relationships for diffusion of the charged particles in semiconductors.

Finally, in order to account for the thermal effects in semiconductor devices, the Fourier equation (2.3.5) is chosen. The material density ρ and specific heat capacity C_ρ of the material are assumed to be independent of temperature based on practical device applications [52], [55]. The tensor $\underline{\underline{k}}$ denotes the thermal conductivity tensor, and Q is the volumetric heat source. In order to avoid complicating the model, an approximation is used by not considering the current induced by gradients of the temperature [52]. The coupling between the thermal and electrical components is defined as the pyroelectric effect. It is defined as the ability of certain materials to generate electric charge as a result of change in temperature induced in the material. This phenomenon is considered here since wurtzite lattices like ZnO exhibit both piezo- and pyroelectric effects.

The governing equations are coupled by using the following constitutive relations which are used to describe the direct and converse piezoelectric effects in semiconductors:

$$\underline{\underline{\sigma}} = \underline{\underline{C}}^E\underline{\underline{\varepsilon}} + \underline{\underline{e}}\vec{\nabla}\phi - \underline{\underline{\beta}}\theta\,, \qquad (converse) \tag{2.3.12}$$

$$\vec{D} = \vec{P}_{piezo} - k_0\underline{\underline{\kappa}}\vec{\nabla}\phi + \vec{\gamma}\theta\,. \quad (direct) \tag{2.3.13}$$

In the equation for the converse piezoelectric effect, $\underline{\underline{\sigma}}$ is the Cauchy stress tensor, $\underline{\underline{C}}^E$ is the elastic stiffness tensor for the electrostatic field, ϕ is the electrostatic potential, $\underline{\underline{\varepsilon}}$ is the Euler-Almansi strain tensor, $\underline{\underline{e}}$ is the piezoelectric strain coefficient tensor, $\underline{\underline{\beta}}$ is the thermal stress tensor, and $\theta = T - T_0$ is the temperature deviation from the reference temperature of $300K$.

In the direct piezoelectric effect equation (2.3.13), $\vec{D}$ is dielectric displacement vector, k_0 is the permittivity of vacuum, $\underline{\underline{\kappa}}$ is the relative dielectric tensor of rank 2, $\vec{\gamma}$ is the primary pyroelectric coefficient, and $\vec{P}_{piezo}$ is the polarization vector which accounts for both linear and nonlinear piezoelectric effects. The relationship depicted by the direct piezoelectric effect equation is valid for materials with time-independent permittivity [52]. Since the behaviour of ZnO wurtzite crystal is isotropic on the basal plane [30], $\underline{\underline{\kappa}}$ is considered to be a scalar quantity [52].

Traditionally, the linear piezoelectric effect has been studied extensively in literature ([18], [31], [36], and references therein), where the polarization vector $\vec{P}_{piezo}$ is given by the product of the first order piezoelectric strain coefficients times the Euler-Almansi strain tensor components. For example, for the linear effect along the c-axis of the NW,

$$\vec{P}_{piezo,lin} = \begin{bmatrix} e_{15}\varepsilon_{zx} \\ e_{15}\varepsilon_{yz} \\ e_{31}(\varepsilon_x + \varepsilon_y) + e_{33}\varepsilon_z \end{bmatrix}, \tag{2.3.14}$$

where e_{15}, e_{31}, and e_{33} are the only three independent piezoelectric strain coefficients as a result of the crystal symmetry in the wurtzite phase of hexagonal ZnO

[30]. However, recently it has been observed that contribution of the second order piezoelectric terms in the polarization vector along the c-axis of the ZnO NW (the nonlinear piezoelectric effect) can predict results with opposite signs for polarization on the NW under compressive/tensile strain, compared to the linear piezoelectric model [37], [38]. For quantum dots such nonlinear effects have been studied in [56].

The nonlinear model of the piezoelectric polarization vector is given by the following equation:

$$\vec{P}_{piezo} = \vec{P}_{piezo,lin} + \begin{bmatrix} 0 \\ 0 \\ P^{sp}_{piezo} + e_{311}\left(\frac{\varepsilon_x+\varepsilon_y}{2}\right)^2 + e_{333}\varepsilon_z^2 + e_{313}\frac{\varepsilon_x+\varepsilon_y}{2}\varepsilon_z \end{bmatrix}, \tag{2.3.15}$$

where the second order piezoelectric strain coefficients are given by e_{311} for double strains on the growth plane, e_{333} for strains perpendicular to the plane, and e_{313} for the combination of parallel and perpendicular strains. In addition, P^{sp}_{piezo} is the spontaneous polarization. The strongest nonlinearities in the NW are observed along the direction of the growth, i.e., the c-axis, and therefore nonlinearities arising from shear strains are ignored [30].

Even though both the stationary and the time-dependent forms of the electromechanical model has been studied extensively in the multi-dimensional case for both ceramics and nanomaterials, a proper time-dependent mathematical model of the TEM system has not been examined yet. It has been known that time-dependent temperature variation in some nanomaterials coupled with their semiconducting properties, successfully generate electric polarization and charge

separation in low dimensional nanostructures (0-D, 1-D, and 2-D nanostructures, such as quantum dots, nanowires, and nanosheets, respectively) [57] fabricated using these materials. Therefore, it is anticipated that introducing time dependence in the TEM coupled system will further enhance the charge separation inside the nanomaterial, thereby increasing current flow in the nanogenerator. In addition, accounting for the decay of excess charge carriers over time in the current continuity equations is expected to give a more realistic model of current generation inside the nanogenerator.

2.4 Boundary Conditions

The M-S interfaces are assumed to be quasi neutral with Schottky barriers. The Schottky barrier heights are regulated by the polarization charges generated at the ends of the NW. The interfaces are also assumed to be in thermal equilibrium, thus satisfying the mass action formula given by $np = n_i^2$, where n_i is the intrinsic carrier concentration. Charge neutrality conditions are also applied at the boundaries, which means that the sum of the charges associated with the carriers must equal zero: $p - n + N = 0$. Here, N is the doping concentration function for the n-doped NW. It can be described approximately using the following Gaussian function [36]:

$$N = N_{Dn} + N_{Dn-max}\, e^{\left(\frac{z-l\times 0.5}{ch}\right)^2}, \tag{2.4.1}$$

where N_{Dn} is the n-type background doping concentration, N_{Dn-max} is the maximum donor doping concentration, ch controls the spreading width of the doping

concentration, l is the length of the ZnO NW, and z represents the positive z-axis of the Cartesian plane. See Figure C.1 in Appendix C for the plot.

Using the mass action formula and the charge neutrality condition, the following carrier concentrations are applied at the M-S interfaces:

$$p = \frac{-N + \sqrt{N^2 + 4n_i^2}}{2}; \;\; n = \frac{N + \sqrt{N^2 + 4n_i^2}}{2} \,. \tag{2.4.2}$$

Boundary condition for the electrostatic potential is given by [36], [52]:

$$\phi = V + \frac{k_B T_0}{q} ln \left(\frac{N + \sqrt{N^2 + 4n_i^2}}{2n_i} \right) \,. \tag{2.4.3}$$

For the elastic displacement, homogeneous Dirichlet boundary conditions are used. For the Fourier equation, a steady Dirichlet boundary condition of $320\ K$ is chosen. On the surface of the nanowire, a zero-flux boundary condition of the following form is applied:

$$-\vec{n} \cdot \vec{\Gamma} = \vec{0} \,, \tag{2.4.4}$$

where $\vec{n}$ is the outward unit normal vector and $\vec{\Gamma}$ is the conservative flux vector.

2.5 Initial Conditions

Initial values for the system variables are determined by first solving the stationary problem and using the solution as an estimate for the initial values of the time-dependent system. The stationary equations are constructed by setting the time derivatives in equations (2.3.1) - (2.3.5) to zero, as illustrated below:

$$\frac{1}{\rho}\vec{\nabla}\cdot\underline{\underline{\sigma}} = 0\,, \tag{2.5.1}$$

$$\vec{\nabla}\cdot\vec{D} = q(p-n+N)\,, \tag{2.5.2}$$

$$\frac{1}{q}\vec{\nabla}\cdot\vec{J_n} + U_n = 0\,, \tag{2.5.3}$$

$$-\frac{1}{q}\vec{\nabla}\cdot\vec{J_p} + U_p = 0\,, \tag{2.5.4}$$

$$\frac{1}{C\rho}(\underline{\underline{k}}\nabla^2 T) + \frac{1}{C\rho}Q = 0\,. \tag{2.5.5}$$

For details on computing the stationary solution, see section 4.1. The initial values thus chosen were also ensured to be consistent with the boundary conditions applied at $z = 0$.

Chapter 3

Drift-Diffusion-Poisson System as a Building Block for Semiconductors

The drift-diffusion-Poisson system of equations has been classically used to define the fundamental properties of semiconductor devices. It consists of two parabolic drift-diffusion equations for electron and hole concentrations for the bipolar semiconductor model, and the elliptic Poisson equation accounting for the electrostatic potential. This chapter includes an outline of the well-posedness of the drift-diffusion-Poisson model for the unipolar semiconductor and the discretized model for the bipolar case. Some of the most recent studies conducted using this model include [58], [59], [60], [61].

3.1 Well-Posedness of the Problem

Mathematical models cannot always fully predict the behaviour of physical phenomena due to various limitations on even the best models, and often it is difficult to prove well-posedness of an elaborate model. A mathematical model is considered well-posed if there exists a unique solution whose behaviour changes continuously with the initial conditions [62]. Determining well-posedness of a material is of mathematical importance only since physically a unique solution

always exists. The extent to which a model is well-posed determines how effective it is to depict the physical phenomenon. In the case of semiconductor devices, the drift-diffusion-Poisson type models are usually analysed in order to determine well-posedness [52], [62], [63].

In this section, the well-posedness of a drift-diffusion-Poisson system of a unipolar semiconductor model is outlined as an example. Details of the exactness and uniqueness proofs can be found in [63]. This particular model consists of the electron continuity equation $n(x,t)$, Poisson equation $V(x,t)$, and the equation for electron temperature $\theta(x,t)$. This unipolar drift-diffusion-Poisson model is a special case of the model considered in Chapter 2:

$$\frac{\partial n}{\partial t} - \vec{\nabla} \cdot (\vec{\nabla}(n\theta) + n\vec{\nabla}V) = 0\,, \tag{3.1.1}$$

$$\vec{\nabla} \cdot (k(n)\vec{\nabla}\theta) = \frac{n}{\tau}(\theta - \theta_L(x))\,, \tag{3.1.2}$$

$$-\lambda^2\nabla^2 V = n - C(x) \quad \text{in } \Omega, t > 0\,. \tag{3.1.3}$$

These equations hold in the bounded domain $\Omega \subset \mathbb{R}^d (d \geqslant 1)$ where $k(n)$ is the thermal conductivity, $\theta_L(x)$ is the lattice temperature, $C(x)$ is the doping profile, τ is the relaxation time, and λ is the Debye length. The initial and boundary conditions are as follows:

$$n(0) = n_l \quad \text{in } \Omega\,, \tag{3.1.4}$$

$$n = n_D, \quad \theta = \theta_D, \quad V = V_D \qquad \text{on } \Gamma_D\,, \tag{3.1.5}$$

$$\vec{\nabla}n \cdot \nu = \vec{\nabla}\theta \cdot \nu = \vec{\nabla}V \cdot \nu = 0 \qquad \text{on } \Gamma_N\,, \tag{3.1.6}$$

where it is assumed that the boundary $\partial\Omega\,\epsilon\,C^{0,1}$ is divided into Γ_D and Γ_N and $\partial\Omega = \Gamma_D \cup \Gamma_N, \Gamma_D \cap \Gamma_N = , \Gamma_N$ is closed, the $(d-1)$-dimensional Lebesgue measure of Γ_D is positive, and ν is the exterior unit normal vector on $\partial\Omega$.

The existence theorem is given by [63]: Let $\Omega \subset \mathbb{R}^d (d \geqslant 1)$ be a bounded domain with $\partial\Omega\,\epsilon\,C^{0,1}, T, \tau, \lambda > 0$, and let $k\,\epsilon\,C^1([0,\infty])$ such that there exist k_0, k_1, n_*, $n^* > 0$ with:

$$\begin{aligned} &\text{(i) } k(z) > 0 \text{ for all } z > 0 \\ &\text{(iI) either } k(x) \geqslant k_0 \text{ for all } z \geqslant 0, \text{ or } k(z) = z \text{ for all } 0 \leqslant z \leqslant n_* \\ &\text{(iii) } k(z) \geqslant k_1 z \text{ for all } z \geqslant n_* \end{aligned} \tag{3.1.7}$$

Furthermore, it is also assumed that the boundary data satisfy the following:

$$\begin{aligned} &n_D, V_D \epsilon L^2(0,T;H^1(\Omega)), \quad \theta_D \epsilon L^q(0,T;W^{1,q}(\Omega)), \\ &n_D, \theta_D \epsilon L^\infty(0,T;L^\infty(\Omega)), \quad \inf_{\Omega_T} n_D > 0, \inf_{\Omega_T} \theta_D > 0, \end{aligned} \tag{3.1.8}$$

and the initial data is assumed to satisfy the following conditions:

$$n_l, \theta_L C \epsilon L^\infty(\Omega), \inf_\Omega n_l > 0, \inf_\Omega \theta_L > 0, \inf_\Omega C(x) > 0\,. \tag{3.1.9}$$

Then, there exists a weak solution $(n, \theta, V)\,\epsilon\,L^2(0,T;H^1(\Omega))^3$ to (3.1.1) - (3.1.6) satisfying $\frac{\partial n}{\partial t}\,\epsilon\,L^2(0,T;H^{-1}(\Omega \cup \Gamma_N))$ and:

$$0 \leqslant n(t) \leqslant K_0 e^{\beta t}, 0 < m \leqslant \theta(t) \leqslant M \text{ in } \Omega, t\,\epsilon\,(0,T)\,. \tag{3.1.10}$$

The proof of this existence theorem is based on the Leray-Schauder fixed-point theorem [64] and the Stampacchia truncation method [64]. The Leray-Schauder fixed-point theorem states that if D is a non-empty, convex, bounded and closed subset of Banach space B and $T : D \to D$ is a compact and continuous map, then T has a fixed point in D. The Stampacchia truncation step is needed in the diffusion coefficients of $\vec{\nabla} \cdot (\theta \vec{\nabla} n)$ and $\vec{\nabla} \cdot (k(n) \vec{\nabla} \theta)$ to make these expressions uniformly elliptic.

The uniqueness theorem is given by [63]: Let the assumptions of the existence theorem hold, and let k be locally Lipschitz continuous on $[0, \infty)$. Then, there exists a unique solution (n, θ, V) to (3.1.1) - (3.1.6) in the class of bounded weak solutions satisfying $n \, \epsilon \, L^{\infty}(0, T; W^{1,\infty}(\Omega))$, where $p > 2$ if $d = 2$ and $p \geqslant d$ if $d \geqslant 3$.

The proof is started by assuming (n_1, θ_1, V_1) and (n_2, θ_2, V_2) as solutions to the system using the conditions stated in the theorem. At first an estimate of the quantity $\nabla(\theta_1 - \theta_2)$ is derived by assuming the test function $\theta_1 - \theta_2$ using weak formulations of the two solutions of θ. Next an estimate of $n_1 - n_2$ is determined satisfying the two assumed solutions of n. These estimates are combined and the uniqueness of the solution is proved by applying Hölder's inequality with $p > 2$, Sobolev embedding $H^1(\Omega) \to L^q(\Omega)$, the Poincaré inequality [65], and the Gronwall Lemma [66].

3.2 Discretized Model

The equations describing the basic charge transport model in bipolar semiconductors are given by the following drift-diffusion-Poisson system:

$$-\kappa\nabla^2\phi - q(p - n + N) = 0\,, \tag{3.2.1}$$

$$\frac{\partial n}{\partial t} = \frac{1}{q}\vec{\nabla}\cdot\vec{J}_n + U_n\,, \tag{3.2.2}$$

$$\frac{\partial p}{\partial t} = -\frac{1}{q}\vec{\nabla}\cdot\vec{J}_p + U_p\,, \tag{3.2.3}$$

$$\vec{J}_n = qn\mu_n\vec{E} + qD_n\vec{\nabla}n\,, \tag{3.2.4}$$

$$\vec{J}_p = qp\mu_p\vec{E} - qD_p\vec{\nabla}p\,. \tag{3.2.5}$$

Different models governing these equations have been analyzed for p-n junctions [67] and cylindrical coordinate systems [68] using the finite difference method. As the first steps in this section, the general approach to solving these equations using finite difference method is outlined. The generalized boundary conditions are written in the following manner:

$$\phi = \phi_{applied} + \phi_{built-in}\,, \tag{3.2.6}$$

$$n = \frac{\sqrt{N^2 + 4n_i^2} + N}{2}\,, \tag{3.2.7}$$

$$p = \frac{\sqrt{N^2 + 4n_i^2} - N}{2}\,, \tag{3.2.8}$$

where ϕ is the electrostatic potential, and n and p are the electron and hole carrier concentrations, respectively. For the derivation of the boundary conditions for n

and p, see section 2.4. At the surface of the nanowire, Neumann boundary conditions are applied. These conditions, as per the following equations, imply no surface charges (i.e., the normal component of the electrostatic field is zero) and no current flow through the surface:

$$\vec{\nabla} \cdot \vec{\phi} = 0\,, \tag{3.2.9}$$

$$\vec{\nabla} \cdot \vec{n} = 0\,, \tag{3.2.10}$$

$$\vec{\nabla} \cdot \vec{p} = 0\,. \tag{3.2.11}$$

The following scheme is used to discretize the spatial dimensions:

FIGURE 3.1: 1-D illustration of the adopted nomenclature for finite differences (e.g. [68])

The drift-diffusion-Poisson system is discretized on a 2-D domain using the x and z Cartesian coordinates. The approximate algebraic equations are constructed using the Taylor series expansion. For the Poisson equation (3.2.1), the finite difference approximation at all the inner grid points is given by [52]:

$$\frac{\frac{\partial\phi}{\partial x}\Big|_{i+1/2,j} - \frac{\partial\phi}{\partial x}\Big|_{i-1/2,j}}{\Delta x_i^{avg}} + \frac{\frac{\partial\phi}{\partial z}\Big|_{i,j+1/2} - \frac{\partial\phi}{\partial z}\Big|_{i,j-1/2}}{\Delta z_j^{avg}} = -\frac{q}{\kappa}(p_{i,j} - n_{i,j} + N_{i,j})\,,$$

which is followed by:

$$\frac{\frac{\phi_{i+1,j}-\phi_{i,j}}{\Delta x_i} - \frac{\phi_{i,j}-\phi_{i-1,j}}{\Delta x_{i-1}}}{\Delta x_i^{avg}} + \frac{\frac{\phi_{i,j+1}-\phi_{i,j}}{\Delta z_j} - \frac{\phi_{i,j}-\phi_{i,j-1}}{\Delta z_{j-1}}}{\Delta z_j^{avg}} = -\frac{q}{\kappa}(p_{i,j} - n_{i,j} + N_{i,j}), \quad (3.2.12)$$

where $\Delta x = x_{i+1} - x_i$, $\Delta x_i^{avg} = \frac{\Delta x_i - \Delta x_{i-1}}{2}$, $\Delta z = z_{j+1} - z_j$, and $\Delta z_j^{avg} = \frac{\Delta z_j - \Delta z_{j-1}}{2}$. Time-dependence in the Poisson equation is accounted for by differentiating (3.2.1) with respect to time and by substituting the algebraic difference equations for $\frac{\partial n}{\partial t}$ and $\frac{\partial p}{\partial t}$ into the right hand side of equation (3.2.12) [52].

In order to solve the continuity equations numerically, conservative schemes [69] are applied by subdividing the computational domain in between the grid points. The continuity equations are discretized on the grid nodes of a uniform mesh, which requires the current densities to be determined on the mid-points of neighbouring grid nodes. The equations are evaluated at these mid-points by using interpolation schemes. That is why in order to calculate the current densities, the carrier concentrations also have to be evaluated at the mid-points. The finite difference discretization requires that the mobility μ, electrostatic field $\vec{E}$, Einstein relationships for semiconductors $D_{n/p}$ (see section 2.3 for details), and the current densities $\vec{J}_{n/p}$ are constant within the interval between each grid points, eg., $[x_i, x_{i+1}] \subset [0, L_x]$. In order to be consistent with Poisson equation, it is commonly assumed that the electrostatic potential ϕ varies linearly between adjacent grid points [69]. The current densities are evaluated by using the Scharfetter-Gummel approximation for constant mobility and diffusion [52]. This method is numerically effective when the changes in carrier concentrations are assumed to be large on the computational domain. The Scharfetter-Gummel approximation uses a weighted difference approach instead of central or upwind differences because

the latter approaches can generate nonphysical solutions for carrier concentrations and electrostatic potential unless extremely fine mesh is used [68], [69]. The stationary part of the continuity equations for electrons is given by [52]:

$$\frac{(J_{nx})\Big|_{i+1/2,j} - (J_{nx})\Big|_{i-1/2,j}}{q\Delta x_i^{avg}} + \frac{(J_{nz})\Big|_{i,j+1/2} - (J_{nz})\Big|_{i,j-1/2}}{q\Delta z_j^{avg}} + U_n\Big|_{i,j} = 0\,. \tag{3.2.13}$$

Similarly, for holes [52]:

$$\frac{(-J_{px})\Big|_{i+1/2,j} - (-J_{px})\Big|_{i-1/2,j}}{q\Delta x_i^{avg}} + \frac{(-J_{pz})\Big|_{i,j+1/2} - (-J_{pz})\Big|_{i,j-1/2}}{q\Delta z_j^{avg}} + U_p\Big|_{i,j} = 0\,, \tag{3.2.14}$$

where the algebraic equations for the current density components are given using the Scharfetter-Gummel approximation [70]:

$$\begin{aligned} J_{nx}\Big|_{i+1/2,j} =& D_n\Big|_{i+1/2,j} \frac{B\left(\frac{\phi_{i,j}-\phi_{i+1,j}}{k_BT/q}\right) n_{i,j} - B\left(\frac{\phi_{i+1,j}-\phi_{i,j}}{k_BT/q}\right) n_{i+1,j}}{\Delta x_i} \\ &+ \Delta x_i \left(\frac{1}{2} coth\left(\frac{\phi_{i+1,j}-\phi_{i,j}}{2k_BT/q}\right) - \frac{k_BT/q}{\phi_{i+1,j}-\phi_{i,j}}\right) \frac{\partial}{\partial x} J_{nx}\Big|_{i+1/2,j}\,, \end{aligned} \tag{3.2.15}$$

$$\begin{aligned} J_{nz}\Big|_{i,j+1/2} =& D_n\Big|_{i,j+1/2} \frac{B\left(\frac{\phi_{i,j}-\phi_{i,j+1}}{k_BT/q}\right) n_{i,j} - B\left(\frac{\phi_{i,j+1}-\phi_{i,j}}{k_BT/q}\right) n_{i,j+1}}{\Delta z_j} \\ &+ \Delta z_j \left(\frac{1}{2} coth\left(\frac{\phi_{i,j+1}-\phi_{i,j}}{2k_BT/q}\right) - \frac{k_BT/q}{\phi_{i,j+1}-\phi_{i,j}}\right) \frac{\partial}{\partial z} J_{nz}\Big|_{i,j+1/2}\,, \end{aligned} \tag{3.2.16}$$

$$J_{px}\Big|_{i+1/2,j} = D_p\Big|_{i+1/2,j} \frac{B\left(\frac{\phi_{i,j}-\phi_{i+1,j}}{k_BT/q}\right) p_{i+1,j} - B\left(\frac{\phi_{i+1,j}-\phi_{i,j}}{k_BT/q}\right) p_{i,j}}{\Delta x_i} + \Delta x_i \left(\frac{1}{2} coth\left(\frac{\phi_{i,j}-\phi_{i+1,j}}{2k_BT/q}\right) - \frac{k_BT/q}{\phi_{i,j}-\phi_{i+1,j}}\right) \frac{\partial}{\partial x} J_{px}\Big|_{i+1/2,j} \tag{3.2.17}$$

,

$$J_{pz}\Big|_{i,j+1/2} = D_p\Big|_{i,j+1/2} \frac{B\left(\frac{\phi_{i,j}-\phi_{i,j+1}}{k_BT/q}\right) p_{i,j+1} - B\left(\frac{\phi_{i,j+1}-\phi_{i,j}}{k_BT/q}\right) p_{i,j}}{\Delta z_j} + \Delta z_j \left(\frac{1}{2} coth\left(\frac{\phi_{i,j}-\phi_{i,j+1}}{2k_BT/q}\right) - \frac{k_BT/q}{\phi_{i,j}-\phi_{i,j+1}}\right) \frac{\partial}{\partial z} J_{pz}\Big|_{i,j+1/2}, \tag{3.2.18}$$

where $B(\chi)$ is the Bernoulli function given by:

$$B(\chi) = \frac{\chi}{e^{\chi}-1}. \tag{3.2.19}$$

Detailed analysis of the exponential difference schemes for nonlocal processes in semiconductors can be found in [52], [69], and [70]. When discretizing the time-dependent system several methods can be applied, such as the fully explicit forward Euler method, semi-implicit time discretization, using an uncoupled scheme with a stabilizing term in the Poisson equation, and the implicit backward Euler method. Most of these methods either have a severe restriction on the time step or display an unphysical oscillatory behaviour making them unsuitable for practical device simulation. In this regard, the implicit backward Euler method gives the most reliable numerical approximation. Even though the method is computationally expensive, it is well known to be unconditionally stable (in the context of linear stability analysis) for arbitrarily large time steps. The main drawback with

this method is having to solve nonlinear algebraic equations at each time step [52], [69].

The general form of equations (3.2.1)-(3.2.3) can be written in the following manner, where functions F, G, and H represent the spatial discretizations formulated using equations (3.2.12)-(3.2.19):

$$0 = F(\phi, n, p)\,, \tag{3.2.20}$$

$$\frac{\partial n}{\partial t} = G(\phi, n, p)\,, \tag{3.2.21}$$

$$\frac{\partial p}{\partial t} = H(\phi, n, p)\,. \tag{3.2.22}$$

The complete discretized equations are as follows:

$$0 = F'(\phi^{m+1}, n^{m+1}, p^{m+1})\,, \tag{3.2.23}$$

$$\frac{n^{m+1} - n^m}{\Delta t^m} = G'(\phi^{m+1}, n^{m+1}, p^{m+1})\,, \tag{3.2.24}$$

$$\frac{p^{m+1} - p^m}{\Delta t^m} = H'(\phi^{m+1}, n^{m+1}, p^{m+1})\,, \tag{3.2.25}$$

where $\Delta t^m = t^{m+1} - t^m$. In the functions G' and H', the generation-recombination $U_{n/p}$ for electrons and holes are evaluated at the m-th time step [52].

In general, the finite difference method approximates solutions to mathematical models at the nodes of the discretized domain of the model. However, the unknown variables have to be twice continuously differentiable, i.e., the PDEs used to model the physical system are in strong form. An alternative to this approach is the finite element method, which obtains the numerical approximation of the solution by converting the PDEs to the weak form, thereby removing the

restriction of twice differentiable on the variables. In finite element method the solutions are computed on each individual element on the domain. This method requires more computational time, but it permits higher order of accuracy on the solution. It is also relatively easier to implement finite element method on an unstructured grid, making this method more flexible than finite difference method [52], [62]. Details on the finite element method are provided in the next chapter. In addition to the finite difference and finite element methods to modelling semiconducting devices, methods such as the Scharfetter-Gummel box-method [71], [72] and the finite volume discretization [73], [74] have been used for semiconductor device modelling.

Chapter 4

Numerical Analysis and Finite Element Discretization

The highly nonlinear nature of the TEM system considered in this thesis, along with coupling between the governing equations (2.3.1) - (2.3.5) makes it difficult to obtain the solution of the equations analytically. Therefore, an iterative method is used to obtain a numerical approximation for the entire coupled system of equations. In order to perform the numerical analysis in this thesis, the software COMSOL Multiphysics is used [75]. COMSOL is a cross-platform software that performs computer-aided simulation using finite element analysis involving complicated geometry, and physical and mathematical nonlinearities in a model.

In COMSOL, the strong form of a PDE is first converted into the weak form internally and then solved by finite element discretization of the model geometry by using the Galerkin method (weighted functions). The resulting system of nonlinear algebraic equations is then solved in COMSOL by using a Newton-Raphson type method. This method of obtaining the solution is sensitive to the initial conditions. If the initial conditions are too far from the computed solution, the nonlinear solver does not converge. The Newton-Raphson method is an iterative method with quadratic convergence, meaning that the square of the error at current iteration is proportional to the error at the next iteration. Below is an outline of the

multivariate Newton-Raphson method.

First, recall the single variable Newton-Raphson method, which is given by:

$$
\begin{aligned}
&F(v) = 0\,, \\
&v^{k+1} = v^k - \frac{F(v^k)}{F'(v^k)}, \qquad k = 0, 1, \cdots
\end{aligned}
$$

Now for the multivariate case in context of the model given by equations (2.3.1) - (2.3.5):

$$
\begin{aligned}
&\vec{F}(\vec{v}) = 0\,, \\
&\vec{v} = [u_x \quad u_z \quad \phi \quad n \quad p \quad T]^T\,, \\
&\vec{F}(\vec{v}) = [F_1(\vec{v}) \quad F_2(\vec{v}) \quad \cdots F_6(\vec{v})]^T\,.
\end{aligned}
\tag{4.0.1}
$$

Using Taylor series expansion (ignoring higher order terms), $F_i(\vec{v})$ is obtained as follows:

$$
F_i(\vec{v}) = F_i(\vec{v^k}) + (v_1 - v_1^k)\frac{\partial F_i(\vec{v^k})}{\partial v_1} + (v_2 - v_2^k)\frac{\partial F_i(\vec{v^k})}{\partial v_2} + \cdots + (v_6 - v_6^k)\frac{\partial F_i(\vec{v^k})}{\partial v_6}\,,
$$

where the vector components $v_1 \ldots v_6$ are given by equation (4.0.1) represent the dependent variables of the TEM system considered in this thesis:

$$
F_i(\vec{v}) = F_i(\vec{v^k}) + (u_x - u_x^k)\frac{\partial F_i(\vec{v^k})}{\partial u_x} + (u_z - u_z^k)\frac{\partial F_i(\vec{v^k})}{\partial u_z} + \cdots + (T - T^k)\frac{\partial F_i(\vec{v^k})}{\partial T}\,.
$$

For subsequent iterations, the preceding equation can be written in the following general form:

$$F_i(\vec{v}) = F_i(\vec{v}^k) + \sum_{j=1}^{n} \left[(v_j^{k+1} - v_j^k) \frac{\partial F_i(\vec{v}^k)}{\partial v_j} \right] , \tag{4.0.2}$$
$$i = 1, \cdots, 6; \quad k = 0, 1, \cdots$$

Using $F_i(\vec{v}) = 0$ in equation (4.0.2),

$$\begin{aligned} &J(\vec{v}^k)(v_j^{k+1} - v_j^k) + \vec{F}(\vec{v}^k) = 0 \,, \\ &v_j^{k+1} = v_j^k - [J(\vec{v}^k)]^{-1} \vec{F}(\vec{v}^k) \,, \end{aligned} \tag{4.0.3}$$

where $J(\vec{v}^k)$ is the Jacobian matrix of the system.

$$J(\vec{v}^k) = \begin{bmatrix} \frac{\partial F_1(\vec{v}^k)}{\partial u_x} & \frac{\partial F_1(\vec{v}^k)}{\partial u_x} & \cdots & \frac{\partial F_1(\vec{v}^k)}{\partial u_x} \\ \frac{\partial F_2(\vec{v}^k)}{\partial u_z} & \frac{\partial F_2(\vec{v}^k)}{\partial u_z} & \cdots & \frac{\partial F_2(\vec{v}^k)}{\partial u_z} \\ \vdots & & \ddots & \vdots \\ \frac{\partial F_6(\vec{v}^k)}{\partial T} & \frac{\partial F_6(\vec{v}^k)}{\partial T} & \cdots & \frac{\partial F_6(\vec{v}^k)}{\partial T} \end{bmatrix} . \tag{4.0.4}$$

Computing inverse of a matrix is computationally demanding, that is why the following approach is used instead. At each step, instead of using equation (4.0.3), the following linearized system of equations is solved, where $\Delta v_j = v_j^{k+1} - v_j^k$ [62]

$$J(\vec{v}^k)\Delta\vec{v} = \vec{F}(\vec{v}) \,. \tag{4.0.5}$$

COMSOL uses a direct or an iterative linear solver to obtain the incremental change in the solution to equation (4.0.5). In this thesis, a direct solver is used because of the fully coupled nature of the governing equations. Direct solvers are suitable for most nonsingular systems. They are robust and are very fast for models like the simple 2-D geometry used in this thesis (see Figure C.2 for details). There are three types of direct solvers in COMSOL - MUMPS, PARDISO, and SPOOLES [75]. These linear system solvers work on general sparse linear systems of the form $A\vec{x} = \vec{b}$ and perform LU factorization on the matrix A. Direct solvers can apply the following optional convergence criterion after the solution step:

$$\rho|M^{-1}(\vec{b} - A\vec{x})| < tol \cdot |M^{-1}\vec{b}|\,. \tag{4.0.6}$$

If the convergence error is greater than the preset value, the solution process is terminated and an error message is generated. For the direct solvers, $M = LU$, where L and U are the LU factors computed by the solver, ρ is the stability constant (default value is 400), and tol is the relative tolerance (default value is 0.01). In terms of the accuracy of the solution, the choice of direct solver is not important, and they differ primarily in their relative speed. The default direct solver MUMPS is chosen as the linear system solver. It works on general systems like $A\vec{x} = \vec{b}$ by using several preordering algorithms to permute the columns in order to minimize the fill-in of the Jacobian matrix.

4.1 Equation-Based Modelling in COMSOL Multiphysics

The governing equations are rearranged according to the General From PDE interface in COMSOL Multiphysics, which is closely related to the conservation laws that define many areas of physics [75]. For a vector of dependent variables $\vec{v}$, the General Form PDE reads as:

$$e_a \frac{\partial^2 \vec{v}}{\partial t^2} + d_a \frac{\partial \vec{v}}{\partial t} + \vec{\nabla} \cdot \vec{\Gamma} = \vec{f}\,, \tag{4.1.1}$$

where $\vec{v} = \{u_x, u_z, \phi, n, p, T\}^T$, $\vec{\Gamma}$ is the conservative flux vector, e_a is the mass coefficient matrix, d_a is the damping/mass coefficient matrix, and $\vec{f}$ is the source term. See Appendix A for details on how the governing equations were incorporated into this form (note that in order to solve the stationary problem, $\frac{\partial^2 \vec{v}}{\partial t^2}$ and $\frac{\partial \vec{v}}{\partial t}$ are assumed to be zero). Internally, equations written in this form are converted to the weak from before processing. This is illustrated in the following example.

Consider the following generalized boundary value problem:

$$\begin{aligned} &-(au')' + bu' + cu = f\,, \\ &u(0) = 0\,, \\ &u(L_x) = 0\,, \end{aligned} \tag{4.1.2}$$

where the coefficients a, b, c can be known constants or simple functions of space or time, f is the source term, and L_x represents the length of the domain in which the boundary value problem is valid. The goal here is to choose an approximate solution u so that the residual $r = -(au')' + bu' + cu - f$ is as small as possible.

Let there be a test function such that $w(x)\ \epsilon\ C^1(0, L_x)$ with homogeneous Dirichlet boundary conditions. Multiplying both sides of equation (4.1.2) by $w(x)$ and integrating the result gives:

$$\int_0^{L_x} w(-(au')' + bu' + cu)dx = \int_0^{L_x} wf dx\,. \tag{4.1.3}$$

Note that by using integration by parts, the first term on the left-hand side of the equation can be written as:

$$\begin{aligned}\int_0^{L_x} -w(au')'dx &= \int_0^{L_x} -wd(au') \\ &= -\left(wau'|_0^{L_x} - \int_0^{L_x} au'w'dx\right) \\ &= \int_0^{L_x} au'w'dx\,.\end{aligned} \tag{4.1.4}$$

This removes the second derivative on u and so equation (4.1.3) can be written as:

$$\int_0^{L_x} au'w'dx + \int_0^{L_x} bwu'dx + \int_0^{L_x} cwudx = \int_0^{L_x} wf dx\,, \tag{4.1.5}$$

which is the weak form of the differential equation. Similar calculations can be shown for the multivariate case pertaining to the system of governing equations for the TEM model, which is how equation (4.1.1) is converted to the weak form in COMSOL.

4.2 Verification Using Method of Manufactured Solutions

Before computing the numerical solution to the mathematical model, it is necessary to verify if the simulation tool works correctly. In this case, the drift-diffusion-Poisson component of the semiconducting NW is analyzed by using the method of manufactured solutions (MMS). This method is used to check whether the simulation tool accurately reproduces the assumed analytical solution [76], [77]. The MMS involves using predefined analytical functions as true solutions to the dependent variables in order to obtain new source terms for the governing equations, and new boundary and initial conditions. These modified governing equations are solved using COMSOL Multiphysics and the numerical solutions are compared to the predefined analytical solutions. The verification was carried out in 1-D (along the c-axis) by using the following equations:

$$-k_0\kappa_{33}\frac{d^2\phi}{dz^2} = q(N+p-n)\,, \tag{4.2.1}$$

$$\frac{\partial n}{\partial t} = \frac{\partial}{\partial z}\cdot\left(-n\mu_n\frac{\partial\phi}{\partial z} + \frac{\mu_n k_B T_0}{q}\frac{\partial n}{\partial z}\right) + U_n\,, \tag{4.2.2}$$

$$\frac{\partial p}{\partial t} = -\frac{\partial}{\partial z}\cdot\left(-p\mu_p\frac{\partial\phi}{\partial z} - \frac{\mu_p k_B T_0}{q}\frac{\partial p}{\partial z}\right) + U_p\,. \tag{4.2.3}$$

Note that for the stationary case, $\frac{\partial n}{\partial t}$ and $\frac{\partial p}{\partial t} = 0$.

The following functions are used as the predefined solutions:

$$\hat{\phi}(z) = sin\left(\frac{z}{15.9155}\right), \tag{4.2.4}$$

$$\hat{n}(z,t) = 10^{10}\left(cos\left(\frac{z}{15.9155}\right) + cos\left(\frac{t}{15.9155}\right)\right), \tag{4.2.5}$$

$$\hat{p}(z,t) = 10^{10}\left(cos\left(\frac{z}{12.72}\right) + cos\left(\frac{t}{12.72}\right)\right). \tag{4.2.6}$$

Note that for the stationary case, $t = 0$.

Below is an illustration of the procedure using the Poisson equation (4.2.1):

Step 1: Add an auxiliary function F to the source term

$$\frac{\partial n}{\partial t} - \frac{\partial}{\partial z}\cdot\left(-n\mu_n\frac{\partial \phi}{\partial z} + \frac{\mu_n k_B T_0}{q}\frac{\partial n}{\partial z}\right) = U_n + F$$

Step 2: Derive the auxiliary function by substituting the assumed solution into the equation

$$\frac{\partial \hat{n}}{\partial t} - \frac{\partial}{\partial z}\cdot\left(-\hat{n}\mu_n\frac{\partial \phi}{\partial z} + \frac{\mu_n k_B T_0}{q}\frac{\partial \hat{n}}{\partial z}\right) = \frac{\hat{n}\hat{p} - n_i^2}{\tau_n(\hat{p}+n_i) + \tau_n(\hat{p}+n_i)} + F$$
$$\Rightarrow F = \frac{\partial \hat{n}}{\partial t} - \frac{\partial}{\partial z}\cdot\left(-\hat{n}\mu_n\frac{\partial \phi}{\partial z} + \frac{\mu_n k_B T_0}{q}\frac{\partial \hat{n}}{\partial z}\right) - \frac{\hat{n}\hat{p} - n_i^2}{\tau_n(\hat{p}+n_i) + \tau_n(\hat{p}+n_i)}$$

Step 3: Substitute the result from *Step 2* into *Step 1*

$$\begin{aligned}\frac{\partial n}{\partial t} - \frac{\partial}{\partial z}\cdot\left(-n\mu_n\frac{\partial \phi}{\partial z} + \frac{\mu_n k_B T_0}{q}\frac{\partial n}{\partial z}\right) =& U_n + \frac{\partial \hat{n}}{\partial t} - \frac{\partial}{\partial z}\cdot\left(-\hat{n}\mu_n\frac{\partial \phi}{\partial z} + \frac{\mu_n k_B T_0}{q}\frac{\partial \hat{n}}{\partial z}\right) \\ & - \frac{\hat{n}\hat{p} - n_i^2}{\tau_n(\hat{p}+n_i) + \tau_n(\hat{p}+n_i)}\end{aligned}$$

Step 4: Repeat the above steps for the rest of the dependent variables

Step 5: Derive the initial and boundary conditions using the assumed solutions (4.2.4), (4.2.5), (4.2.6)

Step 6: Compute the numerical solution

See Appendix B for the results from verification.

Chapter 5

Results and Discussion

The 2-D time-dependent nonlinear piezoelectric model for of the wurtzite ZnO NW is solved using COMSOL Multiphysics. Alongside, the linear piezoelectric model is solved as well in order to compare the results for these two cases. The steady state solution of the two piezoelectric models is computed in order to determine how long it would take for the time-dependent variables to reach the steady state. The solutions to the stationary problem are used to get better initial values for the time-dependent problem. The initial values used for both models and the mesh statistics from finite element discretization of the 2-D NW are provided in Appendix C. Details on how the complete coupled TEM model was built in COMSOL is provided in Appendix D along with the customized computational settings.

The fundamental equations for modelling charge transport within semiconductors is given by the drift-diffusion-Poisson model. This model has been analyzed using a verification method called MMS (as outlined in section 4.2). In this procedure, a set of pre-defined (assumed) analytical solutions of the dependent variables (ϕ, n, and p) are incorporated into the PDEs and the modified equations are solved numerically with the help of appropriate boundary and initial conditions. A successful implementation of this method showed a near perfect match between the approximate and pre-defined solutions of the dependent variables.

This verified the usage of COMSOL Multiphysics as a simulation tool for modelling the classical drift-diffusion-Poisson system for semiconductor devices (see Appendix B for details).

The mathematical model of the TEM system considered in this thesis has been constructed using the governing equations (2.3.1) - (2.3.5), the constitutive relations for the converse and direct piezoelectric effects given by equations (2.3.12) and (2.3.13), respectively, and by applying boundary and initial conditions according to sections 2.4 and 2.5, respectively. The linear model of the piezoelectric effect has been integrated into the TEM system by means of the polarization vector given by equation (2.3.14) and the nonlinear model by using equation (2.3.15). Results from the nonlinear model are summarized on the next page. The time-dependent simulation of the nonlinear piezoelectric effect has been run for $40s$ in steps of $0.005s$. Initial results from simulation were presented in [78].

Electrostatic potential, ϕ:

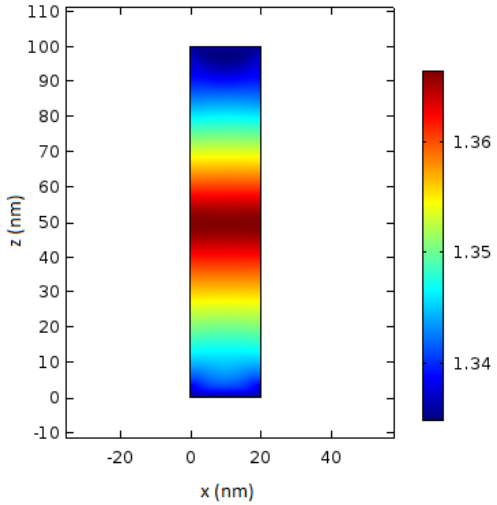

(A) 2-D surface plot of electrostatic potential ϕ

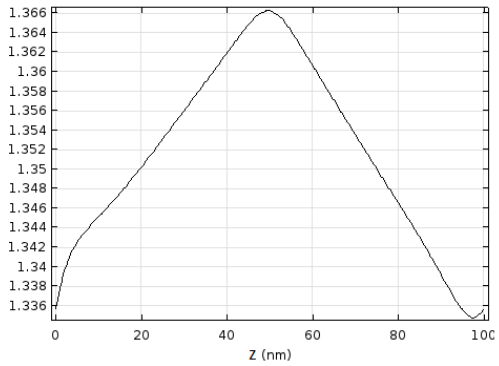

(B) Plot of electrostatic potential ϕ vs. z at $x = 10[nm]$(see Figure C.3)

FIGURE 5.1: Electrostatic potential, $\phi\,[V]$

In Figure 5.1, the 2-D surface plot in (A) depicts the change in electrostatic potential ϕ along the x-z Cartesian plane of the ZnO NW, where the value of ϕ ranges between $1.33478[V] - 1.36637[V]$. The line graph in (B) shows the change in electrostatic potential along the z-axis (which represents the c-axis of the NW). It reflects the shape of the Gaussian doping profile N (given by equation (2.4.1) and Figure C.1). The boundary conditions for ϕ have been applied using equation (2.4.3), where the applied potential $V = 0.8[V]$ based on examples in [18], [36]. The value of ϕ at the boundaries is given by $1.3357[V]$, and this can be seen in the subfigure (B) above. Both of these figures have been generated using data from the the time-dependent simulation at the end of $40s$.

Electron concentration, n:

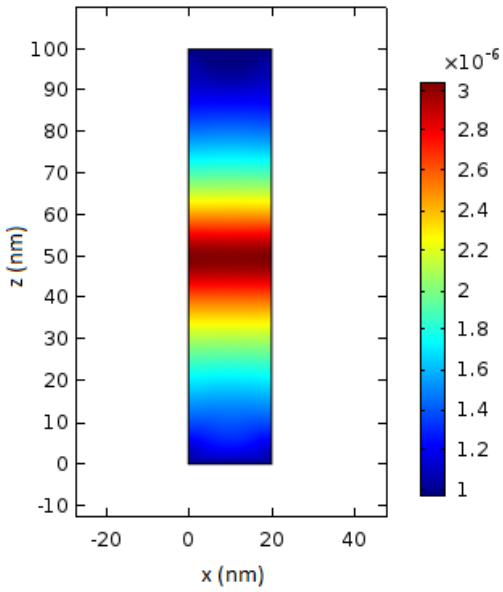

(A) 2-D surface plot of electron concentration n

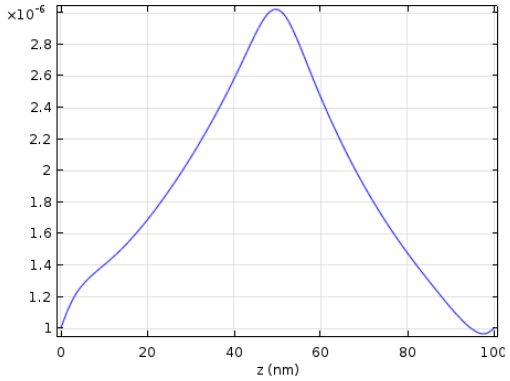

(B) Plot of electron concentration n vs. z at $x = 10[nm]$ (see Figure C.3)

FIGURE 5.2: Electron concentration, n $[1/nm^3]$

Figure 5.2 shows results for the electron concentration n from the time-dependent simulation of the nonlinear model of piezoelectric effect. Both the 2-D surface plot (A) and the line graph (B) have been generated using data from the last time step at $40s$. The surface plot shows variation of the electron concentration throughout the 2-D ZnO NW. The value of n is shown to have a maximum value in the middle of the NW, which is confirmed by the line graph in plot (B). This shape is in agreement with the doping profile N (given by equation (2.4.1) and Figure C.1) that has been formulated for an n-doped semiconductor. The minimum and maximum values of n are given by $9.657 \times 10^{-7}[1/nm^3]$ and $3.036 \times 10^{-6}[1/nm^3]$. The line graph is

also shown to satisfy the Dirichlet boundary condition given by equation (2.4.2), which has numerical value of $1 \times 10^{-6}[1/nm^3]$ at both boundaries.

Hole concentration, p:

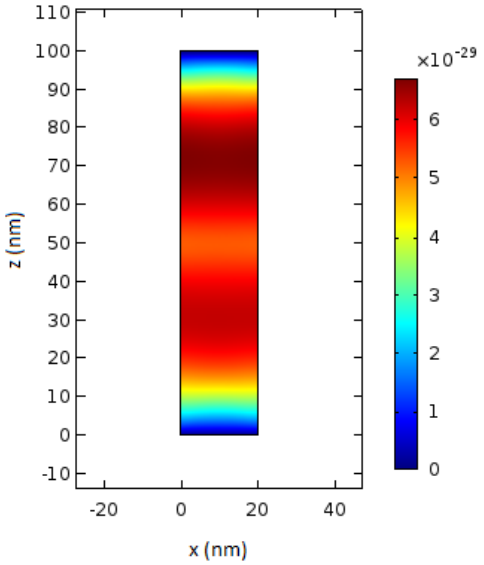

(A) 2-D surface plot of hole concentration p

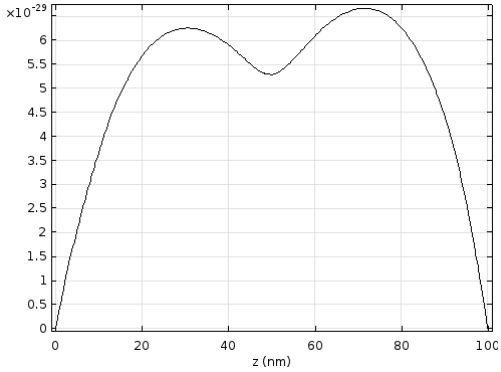

(B) Plot of hole concentration p vs. z at $x = 10[nm]$ (see Figure C.3)

FIGURE 5.3: Hole concentration, p $[1/nm^3]$

In Figure 5.3, the result for hole concentration p at the final step of the time-dependent simulation is shown by means of the 2-D surface plot in (A) and the line graph in (B). The surface plot shows the change in hole concentration on the x-z Cartesian plane of the 2-D ZnO NW, where a minimum value in the hole concentration p is observed. This can be seen clearly in the subfigure (B). The numerical value of p is considerably smaller compared to n (see Figure 5.2) since the model of ZnO NW considered here is doped only with donors impurities. In this regard, the plots for n and p indicate numerical values that are almost opposite of each other which is expected due to the absence of acceptor impurities in the NW and the mass

action formula given by $np = n_i^2$. The minimum and maximum values of p are given by $0[1/nm^3]$ and $6.607 \times 10^{-6}[1/nm^3]$, and the line graph is shown to satisfy the Dirichlet boundary condition given by equation (2.4.2), which has numerical value of $0[1/nm^3]$ at both boundaries.

Hole current density, J_p:

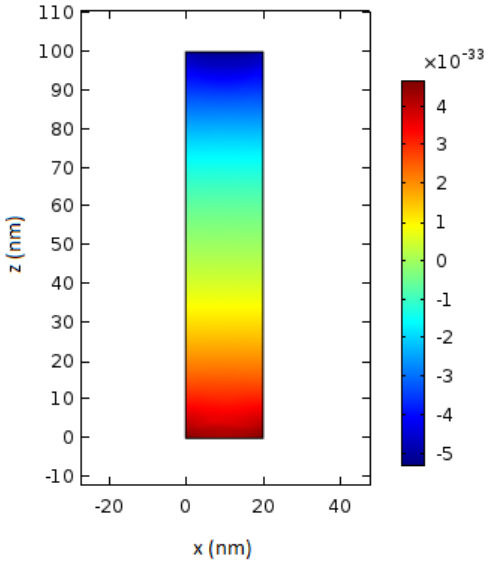

(A) 2-D surface plot of hole current density J_p

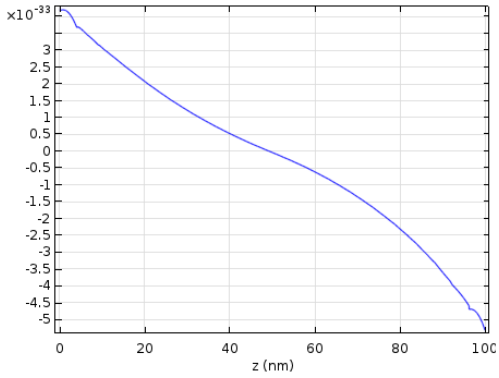

(B) Plot of hole current density J_p vs. z at $x = 10[nm]$(see Figure C.3)

FIGURE 5.4: Hole current density, J_p $[A/nm^2]$

In Figure 5.4, the 2-D surface plot in (A) depicts the change in the hole current density J_p along the x-z Cartesian plane of the ZnO NW. The plot in (B) shows the change in hole current density along the z-axis (which represents the c-axis of the NW). Both of these figures have been generated using results from the the time-dependent simulation at the end of $40s$. The hole current density is shown to decrease along the length of the NW due to absence of donor dopants in the

doping profile. Numerical values of J_p range between -4.647×10^{-33} $[A/nm^2]$ and 5.320×10^{-33} $[A/nm^2]$.

Elastic displacement, u_z:

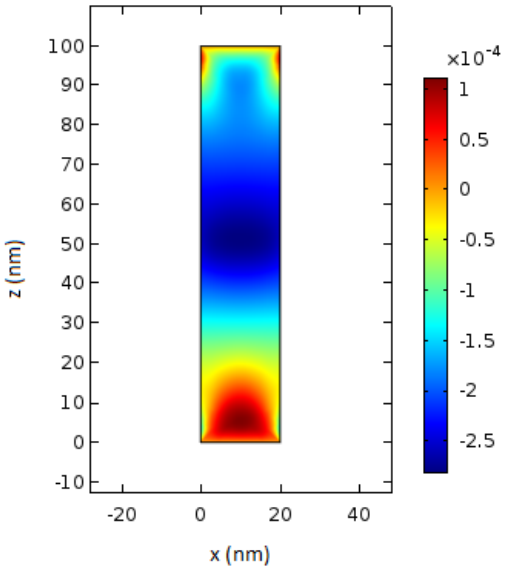

(A) 2-D surface plot of z-component of the elastic displacement u_z

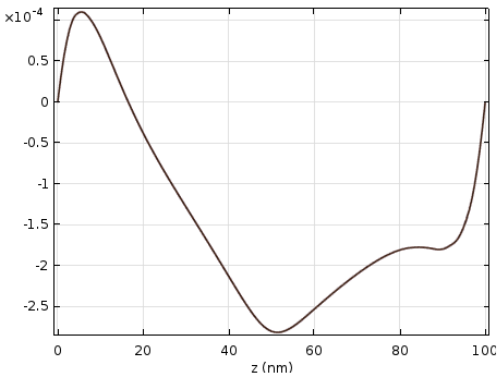

(B) Plot of z-component of the elastic displacement u_z vs. z at $x = 10[nm]$(see Figure C.3)

FIGURE 5.5: Elastic displacement, u_z $[nm]$

Figure 5.5 shows results for z-component of the mechanical elastic displacement, u_z, on the NW during the charge transport process. It represents the deformation of the ZnO NW under zero external stress. The 2-D surface plot shown in (A) depicts the elastic displacement u_z along the x-z Cartesian plane of the ZnO NW. The plot in (B) shows how u_z varies along the vertical cross-section of the NW, i.e., along the c-axis at $x = 10[nm]$. Both of these figures have been generated using data from the the time-dependent simulation at the end of $40s$. Numerical values of u_z range

between -2.817×10^{-4} $[nm]$ and 1.105×10^{-4} $[nm]$. For results of x-component of the displacement, u_x, see Figure C.8 in Appendix C.

Stress, σ_z:

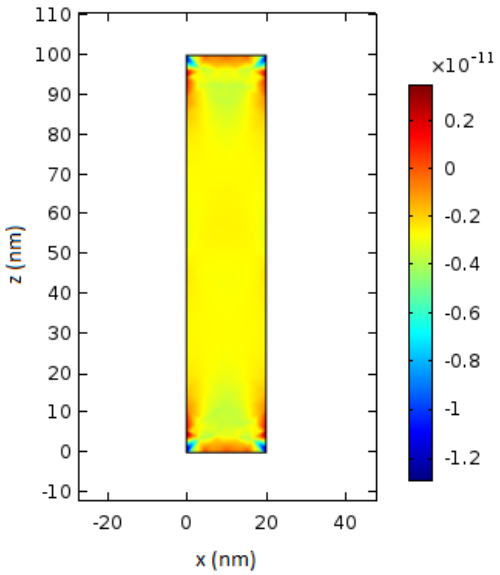

(A) 2-D surface plot of σ_z

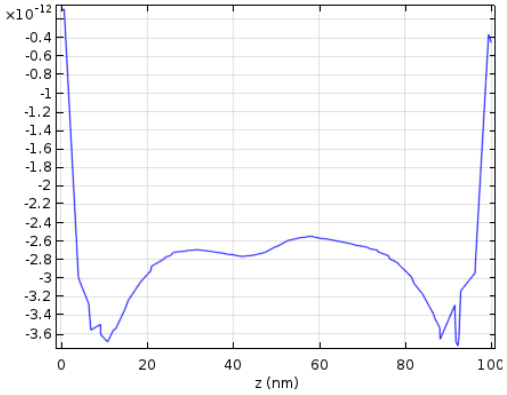

(B) Plot of σ_z vs. z at $x = 10[nm]$(see Figure C.3)

FIGURE 5.6: Stress tensor, $\sigma_z[N/nm^2]$

In Figure 5.6, the 2-D surface plot in (A) depicts the change in the z-component of the stress tensor, σ_z, respectively, along the x-z Cartesian plane of the ZnO NW. The plot in (B) shows the change in σ_z along the z-axis (which represents the c-axis of the NW). The two plots have been generated using data from the the time-dependent simulation at the end of $40s$. The component σ_z has been calculated using equation (A.2.4), which is dependent on the partial derivatives of the elastic displacement components u_x and u_z, and the electrostatic potential ϕ. As a result, computing stress accurately is more difficult. Numerical values of σ_z range between -1.298×10^{-11} $[N/nm^2]$ and 3.441×10^{-12} $[N/nm^2]$.

Stress, σ_x:

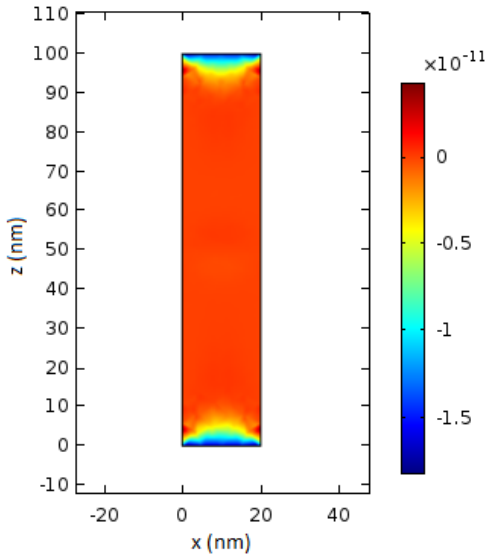

(A) 2-D surface plot of σ_x

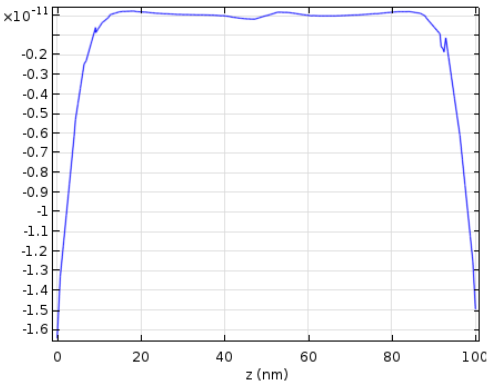

(B) Plot of σ_x vs. z at $x = 10[nm]$ (see Figure C.3)

FIGURE 5.7: Stress tensor, σ_x $[N/nm^2]$

In Figure 5.7, the 2-D surface plot in (A) depicts the change in σ_x, respectively, along the x-z Cartesian plane of the ZnO NW. The plot in (B) shows the change in z component of the stress tensor along the z-axis (which represents the c-axis of the NW). Both of these figures have been generated using data from the the time-dependent simulation at the end of $40s$. The x-component of the stress tensor, σ_x has been calculated using equation (A.2.3), which is dependent on the partial derivatives of the elastic displacement components u_x and u_z, and the electrostatic potential ϕ. Numerical values of σ_x range between -1.828×10^{-11} $[N/nm^2]$ and 4.225×10^{-12} $[N/nm^2]$.

The physical quantities considered in this TEM model account for the primary characteristics of interest in energy harvesting nanodevices (i.e., nanogenerators), such as the drift-diffusion-Poisson and mechanical elastic components. For piezoelectric energy harvesters, it is important to analyse the effect of stress on the output current and voltage in order to determine the efficiency of such devices.

Chapter 6

Conclusion and Future Work

In this thesis, a mathematical model has been applied to study the nonlinear piezoelectric effect in wurtzite ZnO NW doped with donor impurities. The mathematical model implemented is an extension based upon the state of the art research published by Araneo *et al* in 2016, where the stationary TEM system was modelled in 1-D. The novel model used in this thesis has been constructed using a system of fully-coupled nonlinear PDEs representing the time-dependent TEM model of the NW in 2-D. Models of this type, where thermal, electrical, and mechanical components of semiconductor devices are considered, are essential for understanding energy harvesting capabilities of semiconducting NWs. For boundary conditions on the NW, the quasi-neutral condition has been applied at the ends of the NW and a zero flux condition has been applied on the surface of the 2-D model. The governing equations of the model consist of the equation for elastic displacement, Poisson equation, current continuity equations, and the Fourier equation. These equations have been combined with the constitutive relations for direct and converse piezoelectric effects. The nonlinear piezoelectric effect has been taken into account in the Poisson equation by means of the direct piezoelectric effect. In the developed model, the constitutive equations have also accounted for the primary pyroelectric effect along the c-axis of the NW.

This highly nonlinear model has been solved numerically by means of a

variational formulation based on finite element representation. In particular, it has been implemented into the COMSOL Multiphysics solver. The equations were solved on a finely discretized 2-D rectangular domain representing the ZnO NW. The simulation tool was verified by using the main drift-diffusion component of the mathematical model for the 1-D steady state case. In order to compare the results, the linear model for the piezoelectric effect has been solved as well. The model considered in this thesis can be generalized to a 2-D ZnO NW doped with donor impurities. The numerical solution has been computed under the assumptions of an unperturbed state of the NW, i.e., no applied stress, light source to account for carrier generation, and body force. For the model specifications used in this thesis, the results from finite element analysis generated comparable results for the linear and nonlinear piezoelectric models.

This research provides several opportunities for expansion. The mathematical model used in this thesis to describe the piezoelectric effect in the semiconducting wurtzite ZnO NW can be used as a generalized model of the charge transport process inside an unperturbed n-doped ZnO NW. To emphasize this conclusion, the current physical setup can be extended to solve for the M-S-M structure for the complete nanogenerator model, which will account for the bandgap between the gold contacts and ZnO NW. Subsequently, the model can be extended to study the effect of compressive/tensile strain on the M-S-M structure. In addition, instead of using the Fourier equation to depict the thermal component of the mathematical model, the energy balance equation for semiconductors can be used.

The mathematical model presented in this thesis has been constructed by accounting for both the direct and converse piezoelectric effects in a TEM model.

It has been used to study the piezoelectric effect and obtain all principal characteristics of the physical system by using a set of time-dependent nonlinear PDEs with strong coupling on a 2-D ZnO NW doped with donor impurities. The developed variational implementation of this model, based on finite element representation, is amenable to further analysis in the context of energy harvesting and other important applications.

Appendix A

Equations used with General Form PDE

A.1 Tensors and Vectors

The tensors and vectors used to construct the constitutive equations (2.3.12) and (2.3.13) are given below:

$$\underline{\underline{\sigma}} = \begin{bmatrix} \sigma_x & \sigma_{xy} & \sigma_{xz} \\ \sigma_{xy} & \sigma_y & \sigma_{yz} \\ \sigma_{xz} & \sigma_{yz} & \sigma_z \end{bmatrix}, \qquad \underline{\underline{C}}^E = \begin{bmatrix} C_{11} & C_{12} & C_{13} & 0 & 0 & 0 \\ C_{12} & C_{22} & C_{23} & 0 & 0 & 0 \\ C_{13} & C_{23} & C_{33} & 0 & 0 & 0 \\ 0 & 0 & 0 & C_{44} & 0 & 0 \\ 0 & 0 & 0 & 0 & C_{55} & 0 \\ 0 & 0 & 0 & 0 & 0 & C_{66} \end{bmatrix},$$

$$\underline{\underline{e}}^T = \begin{bmatrix} 0 & 0 & 0 & 0 & e_{15} & 0 \\ 0 & 0 & 0 & e_{24} & 0 & 0 \\ e_{31} & e_{32} & e_{33} & 0 & 0 & 0 \end{bmatrix}, \qquad \underline{\underline{\kappa}} = \begin{bmatrix} \kappa_{11} & 0 & 0 \\ 0 & \kappa_{22} & 0 \\ 0 & 0 & \kappa_{33} \end{bmatrix}, \qquad \vec{\gamma} = \begin{bmatrix} 0 & 0 & \gamma_z & 0 & 0 & 0 \end{bmatrix}^T,$$

$$\underline{\underline{\varepsilon}}^T = \begin{bmatrix} \varepsilon_x & \varepsilon_y & \varepsilon_z & 2\varepsilon_{yz} & 2\varepsilon_{zx} & 2\varepsilon_{xy} \end{bmatrix}, \qquad \underline{\underline{\beta}} = \begin{bmatrix} b_{11} & b_{22} & b_{33} & 0 & 0 & 0 \end{bmatrix}.$$

The Cauchy stress tensor $\underline{\underline{\sigma}}$ is a second order stress tensor which accounts for the different stress components inside a material when it is in the deformed state [79]. The tensor $\underline{\underline{C}}^E$ is the elastic stiffness tensor, where the superscript E represents the electrostatic field. For a hexagonal wurtzite structure like ZnO, which is isotropic on the basal plane, the stiffness tensor has only five independent elastic constants: $C_{11} = C_{22}$, C_{12}, $C_{13} = C_{23}$, C_{33} , $C_{44} = C_{55}$, $C_{66} = (C_{11} - C_{22})/2$ [45], [79]. The tensor $\underline{\underline{e}}^T$ is the second order piezoelectric strain coefficient tensor with three independent values: $e_{31} = e_{32}$, e_{33}, $e_{15} = e_{24}$ [30]. The tensor $\underline{\underline{\kappa}}$ contains the dielectric constants (or, relative permittivities) for ZnO. Dielectric constants measure the ability of a substance to store electrical energy in an electric field [45], [79]. These constants are material specific and represent the ratio of material permittivity to the permittivity of free space. The primary pyroelectric coefficient vector $\vec{\gamma}$ can be used to describe the changes produced under a change in temperature, and it is significant only along the c-axis of the NW [30], [80]. In the Euler-Almansi strain tensor $\underline{\underline{\varepsilon}}^T$, each term represents the rate of change of different components of the elastic displacement with respect to the spatial axes and planes. For example: $\varepsilon_x = \partial u_x/\partial x$, $\varepsilon_z = \partial u_z/\partial z$, $\varepsilon_{xz} = (\partial u_x/\partial z + \partial u_z/\partial x)/2$, etc. [81]. The thermal stress tensor $\underline{\underline{\beta}}$ is given by $\underline{\underline{\beta}} = \underline{\underline{C}}^E \underline{\underline{\alpha}}$ [30].

A.2 Elasticity Equation

Recall equation (2.3.1):

$$\frac{\partial^2 \vec{u}}{\partial t^2} = \frac{1}{\rho}\vec{\nabla}\cdot\underline{\underline{\sigma}}\,,$$
$$\frac{\partial^2}{\partial t^2}\begin{bmatrix} u_x \\ u_y \\ u_z \end{bmatrix} = \frac{1}{\rho}\begin{bmatrix} \frac{\partial \sigma_x}{\partial x} + \frac{\partial \sigma_{xy}}{\partial y} + \frac{\partial \sigma_{xz}}{\partial z} \\ \frac{\partial \sigma_{xy}}{\partial x} + \frac{\partial \sigma_y}{\partial y} + \frac{\partial \sigma_{yz}}{\partial z} \\ \frac{\partial \sigma_{xz}}{\partial x} + \frac{\partial \sigma_{yz}}{\partial y} + \frac{\partial \sigma_z}{\partial z} \end{bmatrix},$$

where $\vec{u}$ is the elastic displacement vector, ρ is the material density, and the components of the stress tensor are derived in the following manner using equation (2.3.12):

$$\begin{aligned}
\sigma_x &= C_{11}\varepsilon_x + C_{12}\varepsilon_y + C_{13}\varepsilon_z + e_{31}\frac{\partial \phi}{\partial z} - b_{11}\theta \\
&= C_{11}\frac{\partial u_x}{\partial x} + C_{12}\frac{\partial u_y}{\partial y} + C_{13}\frac{\partial u_z}{\partial z} + e_{31}\frac{\partial \phi}{\partial z} - b_{11}\theta\,, \\
\sigma_y &= C_{12}\varepsilon_x + C_{22}\varepsilon_y + C_{23}\varepsilon_z + e_{32}\frac{\partial \phi}{\partial z} - b_{22}\theta \\
&= C_{12}\frac{\partial u_x}{\partial x} + C_{22}\frac{\partial u_y}{\partial y} + C_{23}\frac{\partial u_z}{\partial z} + e_{32}\frac{\partial \phi}{\partial z} - b_{22}\theta\,, \\
\sigma_z &= C_{13}\varepsilon_x + C_{23}\varepsilon_y + C_{33}\varepsilon_z + e_{33}\frac{\partial \phi}{\partial z} - b_{33}\theta \\
&= C_{13}\frac{\partial u_x}{\partial x} + C_{23}\frac{\partial u_y}{\partial y} + C_{33}\frac{\partial u_z}{\partial z} + e_{33}\frac{\partial \phi}{\partial z} - b_{33}\theta\,, \\
\sigma_{yz} &= 2C_{44}\varepsilon_{yz} + e_{24}\frac{\partial \phi}{\partial y} \\
&= C_{24}\left(\frac{\partial u_y}{\partial z} + \frac{\partial u_z}{\partial y}\right) + e_{24}\frac{\partial \phi}{\partial y}\,,
\end{aligned}$$

$$\begin{aligned}\sigma_{xz} &= 2C_{55}\varepsilon_{xz} + e_{15}\frac{\partial\phi}{\partial x} \\ &= C_{55}\left(\frac{\partial u_x}{\partial z} + \frac{\partial u_z}{\partial x}\right) + e_{15}\frac{\partial\phi}{\partial x}\,, \\ \sigma_{xy} &= 2C_{66}\varepsilon_{xy} \\ &= C_{66}\left(\frac{\partial u_y}{\partial x} + \frac{\partial u_x}{\partial y}\right)\,.\end{aligned}$$

Therefore, for the 2-D case, the stress tensor components are given by:

$$\frac{\partial^2}{\partial t^2}\begin{bmatrix} u_x \\ u_z \end{bmatrix} = \frac{1}{\rho}\begin{bmatrix} \frac{\partial\sigma_x}{\partial x} + \frac{\partial\sigma_{xz}}{\partial z} \\ \frac{\partial\sigma_{xz}}{\partial x} + \frac{\partial\sigma_z}{\partial z} \end{bmatrix}\,,$$

which can be split into the following two equations with respect to the derivatives of u_x and u_z, where the respective right-hand side components are expressed as scalar products:

$$\begin{aligned}\frac{\partial^2 u_x}{\partial t^2} &= \frac{1}{\rho}\left(\frac{\partial\sigma_x}{\partial x} + \frac{\partial\sigma_{xz}}{\partial z}\right)\,, \\ &= \frac{1}{\rho}\begin{bmatrix} \frac{\partial}{\partial x} \\ \frac{\partial}{\partial z} \end{bmatrix} \cdot \begin{bmatrix} \sigma_x \\ \sigma_{xz} \end{bmatrix} \qquad \text{(A.2.1)} \\ \frac{\partial^2 u_z}{\partial t^2} &= \frac{1}{\rho}\left(\frac{\partial\sigma_{xz}}{\partial x} + \frac{\partial\sigma_z}{\partial z}\right)\,, \\ &= \frac{1}{\rho}\begin{bmatrix} \frac{\partial}{\partial x} \\ \frac{\partial}{\partial z} \end{bmatrix} \cdot \begin{bmatrix} \sigma_{xz} \\ \sigma_z \end{bmatrix}\,, \qquad \text{(A.2.2)}\end{aligned}$$

where

$$\sigma_x = C_{11}\frac{\partial u_x}{\partial x} + C_{13}\frac{\partial u_z}{\partial z} + e_{31}\frac{\partial \phi}{\partial z} - b_{11}\theta\,, \tag{A.2.3}$$

$$\sigma_z = C_{13}\frac{\partial u_x}{\partial x} + C_{33}\frac{\partial u_z}{\partial z} + e_{33}\frac{\partial \phi}{\partial z} - b_{33}\theta\,, \tag{A.2.4}$$

$$\sigma_{xz} = C_{55}\left(\frac{\partial u_x}{\partial z} + \frac{\partial u_z}{\partial x}\right) + e_{15}\frac{\partial \phi}{\partial x}\,. \tag{A.2.5}$$

A.3 Poisson Equation

Recall equation (2.3.2):

$$\begin{aligned} &\vec{\nabla}\cdot\vec{D} = q(p - n + N) \\ &\frac{\partial D_x}{\partial x} + \frac{\partial D_y}{\partial y} + \frac{\partial D_z}{\partial z} = q(p - n + N)\,, \end{aligned} \tag{A.3.1}$$

where the components D_x, D_y, and D_z of the dielectric displacement vector are calculated in the following using equation (2.3.13):

$$\begin{bmatrix} D_x \\ D_y \\ D_z \end{bmatrix} = \begin{bmatrix} e_{15}\left(\frac{\partial u_x}{\partial z} + \frac{\partial u_z}{\partial x}\right) \\ e_{24}\left(\frac{\partial u_y}{\partial z} + \frac{\partial u_z}{\partial y}\right) \\ e_{31}\frac{\partial u_x}{\partial x} + e_{32}\frac{\partial u_y}{\partial y} + e_{33}\frac{\partial u_z}{\partial z} \end{bmatrix} - k_0 \begin{bmatrix} k_{11}\frac{\partial \phi}{\partial x} \\ k_{22}\frac{\partial \phi}{\partial y} \\ k_{33}\frac{\partial \phi}{\partial z} \end{bmatrix} + \begin{bmatrix} 0 \\ 0 \\ \gamma_z\theta \end{bmatrix}\,.$$

Therefore, in 2-D:

$$\begin{bmatrix} D_x \\ D_z \end{bmatrix} = \begin{bmatrix} e_{15}\left(\frac{\partial u_x}{\partial z} + \frac{\partial u_z}{\partial x}\right) \\ e_{31}\frac{\partial u_x}{\partial x} + e_{33}\frac{\partial u_z}{\partial z} \end{bmatrix} - k_0 \begin{bmatrix} k_{11}\frac{\partial \phi}{\partial x} \\ k_{33}\frac{\partial \phi}{\partial z} \end{bmatrix} + \begin{bmatrix} 0 \\ \gamma_z\theta \end{bmatrix}\,.$$

A.4 Equation for Electron Continuity

Using equations (2.3.3) and (2.3.10),

$$\begin{aligned}\frac{\partial n}{\partial t} &= \frac{1}{q}\vec{\nabla}\cdot(qn\mu_n\vec{E} + qD_n\vec{\nabla}n) + U_n\,,\\ &= \vec{\nabla}\cdot(-n\mu_n\vec{\nabla}\phi + \frac{\mu_n k_B T}{q}\vec{\nabla}n) + U_n\,,\end{aligned} \tag{A.4.1}$$

where n is the electron concentration, q is the electric charge, μ_n is the electron mobility, k_B is the Boltzmann constant, T is the absolute temperature, ϕ is the electrostatic potential, and U_n is the net generation-recombination for electrons given by equation (2.3.9).

A.5 Equation for Hole Continuity

Using equations (2.3.4) and (2.3.11),

$$\begin{aligned}\frac{\partial p}{\partial t} &= -\frac{1}{q}\vec{\nabla}\cdot\vec{J}_p + U_p\,,\\ &= -\vec{\nabla}\cdot(-p\mu_p\vec{\nabla}\phi - \frac{\mu_p k_B T}{q}\vec{\nabla}p) + U_p\,,\end{aligned} \tag{A.5.1}$$

where p is the hole concentration, q is the electric charge, μ_p is the hole mobility, k_B is the Boltzmann constant, T is the absolute temperature, ϕ is the electrostatic potential, and U_p is the net generation-recombination for holes given by equation (2.3.9).

A.6 Fourier Equation Accounting for Thermal Effects

Recall equation (2.3.5).

$$\begin{aligned}\frac{\partial T}{\partial t} &= \frac{1}{C\rho}(\underline{\underline{k}}\nabla^2 T) + \frac{1}{C\rho}Q \\ &= \frac{1}{C\rho}\vec{\nabla}\cdot\left(\begin{bmatrix} k_{11} & 0 & 0 \\ 0 & k_{22} & 0 \\ 0 & 0 & k_{33}\end{bmatrix}\vec{\nabla}T\right) + \frac{1}{C\rho}Q \\ &= \frac{1}{C\rho}\vec{\nabla}\cdot\begin{bmatrix} -k_{11}\frac{\partial T}{\partial x}\hat{i} \\ -k_{22}\frac{\partial T}{\partial y}\hat{j} \\ -k_{33}\frac{\partial T}{\partial z}\hat{k}\end{bmatrix} + \frac{1}{C\rho}Q\end{aligned} \tag{A.6.1}$$

where T is the absolute temperature, C_ρ is the specific heat capacity of the material, $\underline{\underline{k}}$ is the thermal conductivity tensor, and Q is the source term.

Rearranging equations (A.2.1), (A.2.2), (A.3.1) - (A.6.1) according to the General Form PDE given by equation (4.1.1) gives:

$$\begin{aligned}\frac{\partial^2 u_x}{\partial t^2} - \frac{1}{\rho}\begin{bmatrix}\frac{\partial}{\partial x} \\ \frac{\partial}{\partial z}\end{bmatrix}\cdot\begin{bmatrix}\sigma_x \\ \sigma_{xz}\end{bmatrix} &= 0\,, \\ \frac{\partial^2 u_z}{\partial t^2} - \frac{1}{\rho}\begin{bmatrix}\frac{\partial}{\partial x} \\ \frac{\partial}{\partial z}\end{bmatrix}\cdot\begin{bmatrix}\sigma_{xz} \\ \sigma_z\end{bmatrix} &= 0\,, \\ \vec{\nabla}\cdot\vec{D} &= q(p-n+N)\,,\end{aligned}$$

$$
\begin{aligned}
&\frac{\partial n}{\partial t} - \vec{\nabla} \cdot (-n\mu_n \vec{\nabla}\phi + \frac{\mu_n k_B T}{q}\vec{\nabla} n) = U_n \,, \\
&\frac{\partial p}{\partial t} + \vec{\nabla} \cdot (-p\mu_p \vec{\nabla}\phi - \frac{\mu_p k_B T}{q}\vec{\nabla} p) = U_p \,, \\
&\frac{\partial T}{\partial t} + \frac{1}{C\rho}\vec{\nabla} \cdot \begin{bmatrix} -k_{11}\frac{\partial T}{\partial x}\hat{i} \\ -k_{22}\frac{\partial T}{\partial y}\hat{j} \\ -k_{33}\frac{\partial T}{\partial z}\hat{k} \end{bmatrix} = \frac{1}{C\rho} Q \,,
\end{aligned}
$$

where $\vec{v} = \{u_x, u_z, \phi, n, p, T\}^T$. The governing equations are presented in COMSOL in the aforementioned manner and are converted to the weak from before processing. This has been illustrated with a simplified example in section 4.1.

Appendix B

Results from Verification

In section 4.2 of this thesis, the procedure of verification of the simulation tool using MMS has been outlined with respect to the primary component of the coupled system presented in this thesis, i.e., the drift-diffusion-Poisson model of semiconductors. The numerical solution was computed in COMSOL Multiphysics by using a variational formulation based on finite element representation. The approximate solutions were compared with the test functions given by equations (4.2.4) - (4.2.6). Accuracy of the numerical solution was achieved by refining the grid gradually. The results from verification using MMS showed the assumed solutions of the dependent variables in the model to align with the numerical solution. This demonstrated the accuracy of COMSOL Multiphysics in computing numerical solution to the drift-diffusion-Poisson system used in semiconductor device modelling, thus proving a guidance for systematic analysis with the coupled system.

The following figures show comparisons, based on the MMS approach, between the assumed solutions and numerical approximations of the electron and hole concentrations, n and p.

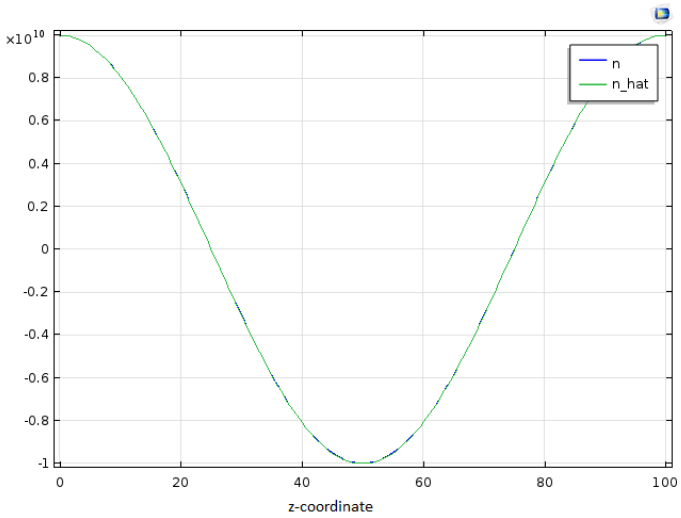

FIGURE B.1: Plot of computed and assumed solutions of electron concentration n vs. z

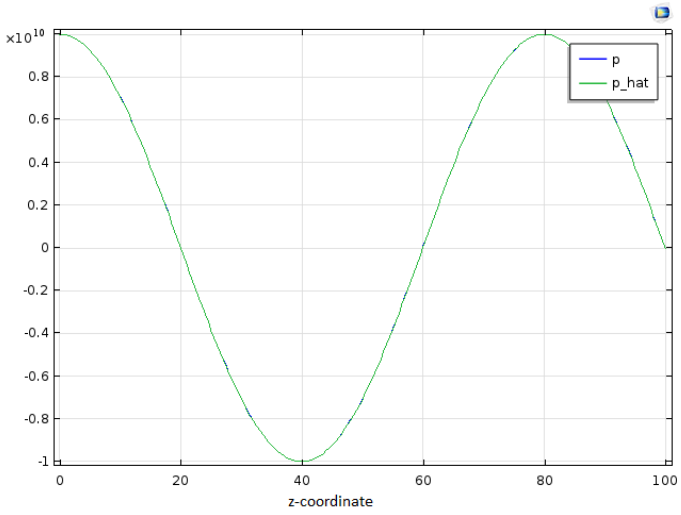

FIGURE B.2: Plot of computed and assumed solutions of electron concentration p vs. z

Below is a plot of the assumed solution chosen for the electrostatic potential ϕ. The order of magnitude of the value of ϕ is negligible compared to that of the carrier concentrations.

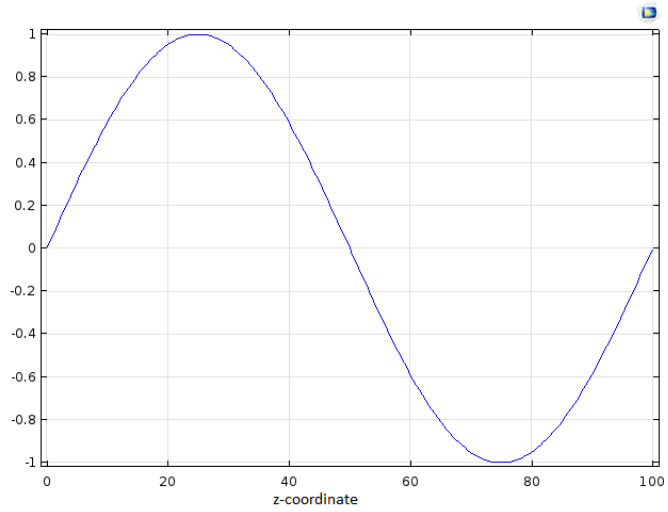

FIGURE B.3: Plot of assumed solution of electrostatic potential $\hat{\phi}$ vs. z

Appendix C

Additional Characteristics and Plots

This appendix contains additional information and results (such as plot of the doping profile, mesh statistics, initial conditions, and additional results) regarding the numerical solution to the TEM mathematical model used in this thesis.

Doping profile as per equation (2.4.1):

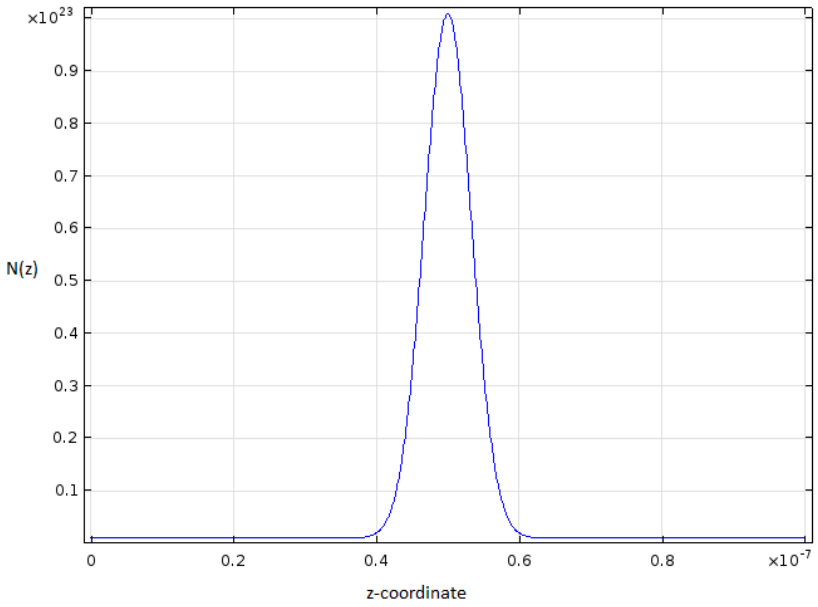

FIGURE C.1: Plot of doping profile N as a function of z

The following figure shows an example of the discretized domain of the 2-D NW using triangular elements. The grid presented is a representation of a trivial triangulation with low aspect ratio of the elements.

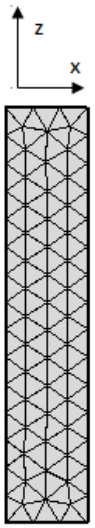

FIGURE C.2: Triangular mesh on ZnO NW for finite element analysis

The figure below is included to depict the line from where the data was used to plot the 2-D line graphs for the dependent variables.

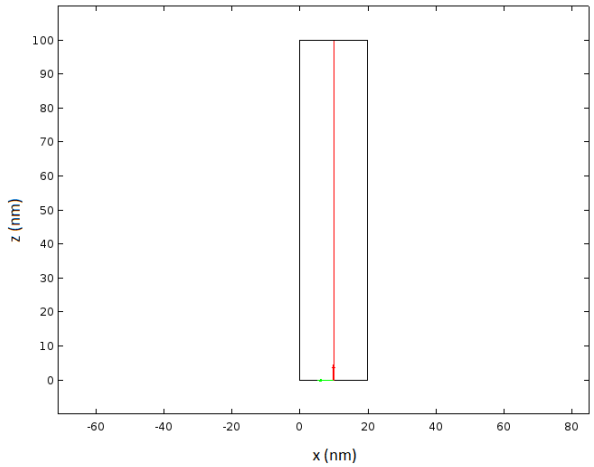

FIGURE C.3: The red line represents the points along the z-axis of the NW at $x = 10[nm]$

The plots in Figures 5.1b, 5.2b, 5.3b, 5.4b, 5.5b, 5.6b, and 5.7b were generated using data from this position.

The following figures show some of the stages of mesh refinement using the mesh statistics and a diagram of the discretized domain as generated by the complete post-computation report in COMSOL Multiphysics.

Description	Value
Minimum element quality	0.7339
Average element quality	0.7488
Number of triangular elements	8
Number of edge elements	10
Number of vertex elements	4

TABLE C.1: Table of mesh statistics of discretized domain for "extremely coarse" mesh in COMSOL

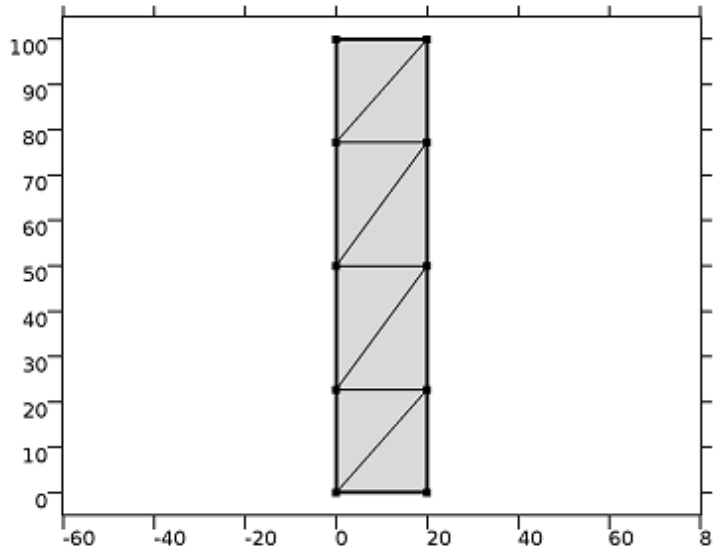

FIGURE C.4: Diagram of discretized domain for "extremely coarse" mesh in COMSOL

Description	Value
Minimum element quality	0.8634
Average element quality	0.9642
Number of triangular elements	42
Number of edge elements	22
Number of vertex elements	4

TABLE C.2: Table of mesh statistics of discretized domain for "coarser" mesh in COMSOL

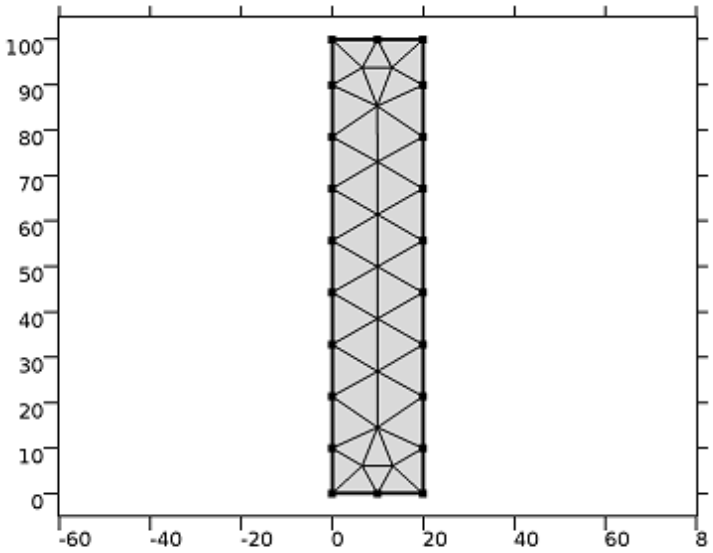

FIGURE C.5: Diagram of discretized domain for "coarser" mesh in COMSOL

Description	Value
Minimum element quality	0.9102
Average element quality	0.9748
Number of triangular elements	122
Number of edge elements	36
Number of vertex elements	4

TABLE C.3: Table of mesh statistics of discretized domain for “normal” mesh in COMSOL

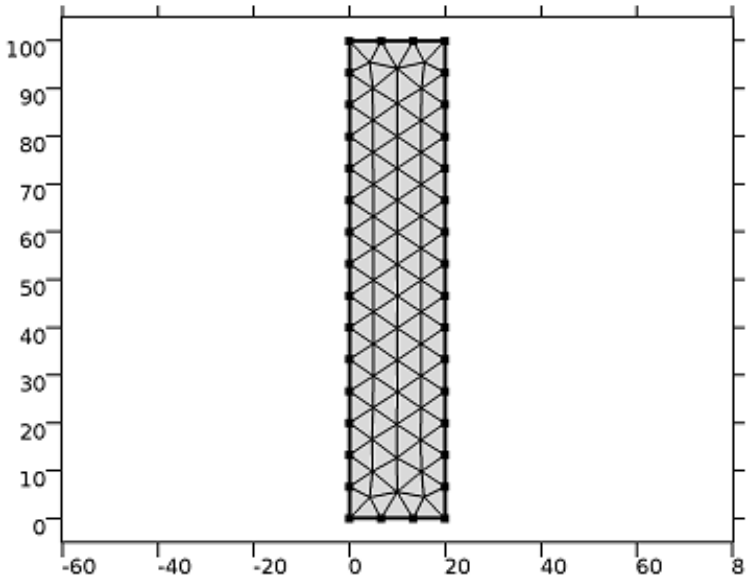

FIGURE C.6: Diagram of discretized domain for "normal" mesh in COMSOL

Description	Value
Minimum element quality	0.8826
Average element quality	0.97
Number of triangular elements	196
Number of edge elements	46
Number of vertex elements	4

TABLE C.4: Table of mesh statistics of discretized domain for “fine” mesh in COMSOL

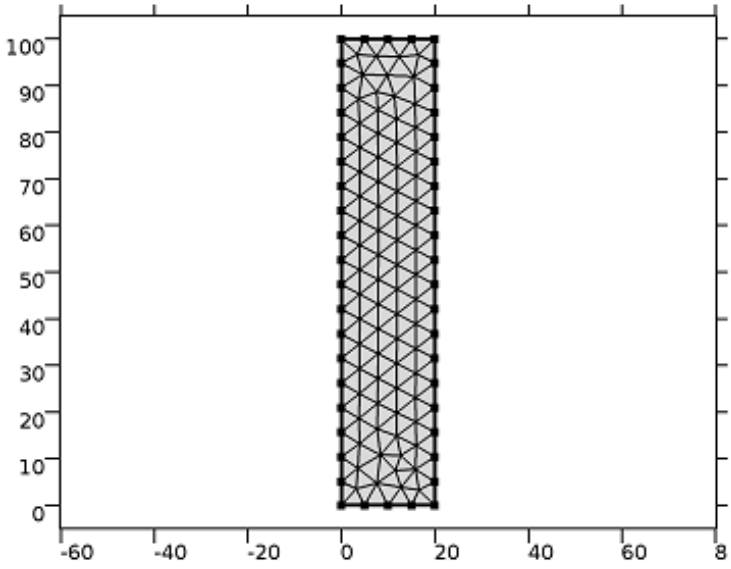

FIGURE C.7: Diagram of discretized domain for "fine" mesh in COMSOL

In Tables C.1 - C.4, the mesh element quality is represented by a dimensionless quantity between 0 and 1, where 0 represents a degenerated element and 1 represents a perfectly regular element. A low mesh element quality can lead to inverted

mesh elements and high condition number for the Jacobian matrix, which in turn can cause convergence issues [75].

The following table contains initial values that have been used for computing solutions to the linear and nonlinear piezoelectric models at time $t = 0$:

Quantity	Linear model	Nonlinear model
$u_x\ [nm]$	0	0.1
$u_z\ [nm]$	0	0.1
$\phi\ [V]$	2	2
$n\ [1/nm^3]$	1×10^{-7}	1×10^{-6}
$p\ [1/nm^3]$	0	1×10^{-29}
$T\ [K]$	300	300
$\frac{\partial u_x}{\partial t}\ [nm/s]$	2	0
$\frac{\partial u_z}{\partial t}\ [nm/s]$	2	0

TABLE C.5: Initial conditions applied during simulation

See section 2.5 for details on how these initial conditions were obtained.

Plot for x-component of the elastic displacement, u_x:

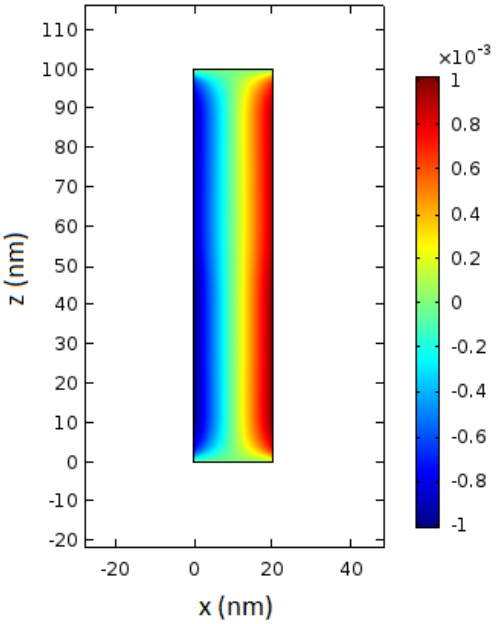

(A) 2-D surface plot of x-component of the elastic displacement u_x

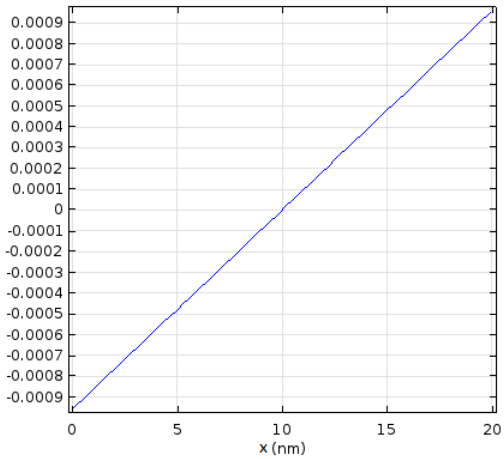

(B) Plot of x-component of the elastic displacement u_x vs. z at $z = 50[nm]$ (see Figure C.9)

FIGURE C.8: Elastic displacement, u_x $[nm]$

Figure C.8 shows results for x-component of the mechanical elastic displacement, u_x, on the NW during the charge transport process. It represents the deformation of the ZnO NW under zero external stress. The 2-D surface plot shown in (A) depicts the elastic displacement u_x along the x-z Cartesian plane of the ZnO NW. The plot in (B) shows how u_x varies along the horizontal cross-section of the NW, i.e., perpendicular to the c-axis at $z = 50[nm]$ (as shown in Figure C.9). Both of these figures have been generated using data from the the time-dependent simulation at the end of $40s$. Numerical values of u_x range between -0.00101 $[nm]$ and 0.00101 $[nm]$.

The following figure is included to depict the line from where the data was used to plot the 2-D line graph for x-component of the elastic displacement in Figure C.8b.

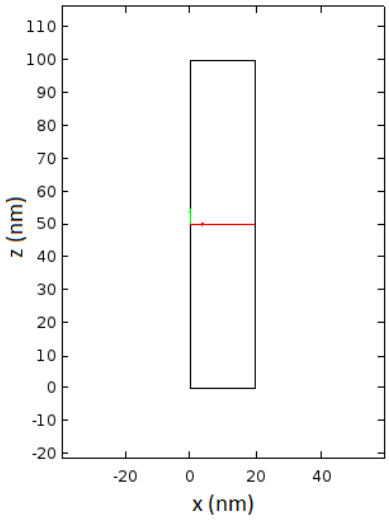

FIGURE C.9: The red line represents the points along the x-axis of the NW at $z = 50[nm]$

Appendix D

Model Building in COMSOL Multiphysics

The solution to the TEM model implemented in this thesis has been computed by obtaining convergence as outlined in Chapter 4. However, it is numerically challenging to solve for the full model in a single step due to the nonlinear and heavily coupled nature of the governing equations. That is why, the TEM model has been built gradually by introducing one equation at a time to the General Form PDE and solving all of the intermediate models by refining the mesh (see Tables C.1 - C.4 and Figures C.4 - C.7 for reference). The combination of equations that were used to build the intermediate model was also important in obtaining convergence. The following flowchart shows the combination of equations that was used to successfully solve the TEM model numerically.

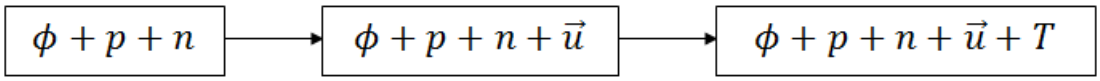

FIGURE D.1: Flowchart showing intermediate steps in building the TEM model in COMSOL using General Form PDE

In the figure above, the dependent variables $\phi, p, n, \vec{u}, T$ represent the governing equations that are primarily associated with (see equations (2.3.1) - (2.3.5)).

The following table contains a list of the customized computational settings for the time-dependent and stationary solvers with respect to the General Form PDE (equation 4.1). These same changes applied while solving for both the linear and nonlinear piezoelectric models. The maximum number of iterations listed below are specific to the "fine" mesh discretization (see Table C.4 and Figure C.7).

Computational settings	Time-dependent solver	Stationary solver
Range	$0 : 0.005 : 40\ [s]$	- -
Relative tolerance	0.0001	
Direct solver	MUMPS	
Memory allocation factor	1.2	
Preordering algorithm	Automatic	
Linear solver	Direct	
Method of termination	Constant (Newton)	
Damping factor	0.6	0.4
Limit on nonlinear convergence rate	0.9	- -
Jacobian update	On every iteration	
Termination technique	tolerance	solution on residual
Tolerance factor	1	
Residual factor	- -	1000
Maximum number of iterations	500	600

TABLE D.1: Computational settings for the time-dependent and stationary solvers

Bibliography

[1] Guozhong Cao and Ying Wang. *Nanostructures and nanomaterials: synthesis, properties, and applications*. World Scientific, 2011.

[2] Chris Binns. *Introduction to nanoscience and nanotechnology*. Wiley, 2010.

[3] Malkiat S. Johal. *Understanding nanomaterials*. CRC Press, 2012.

[4] Zhao Wang et al. "Piezoelectric nanowires in energy harvesting applications". In: *Advances in Materials Science and Engineering* 2015 (2015).

[5] Quan Li. *Nanomaterials for sustainable energy*. Springer, 2016.

[6] Online Etymology Dictionary. *piezo-*. [Online; accessed 23-February-2017]. 2017. URL: http://www.etymonline.com/index.php?term=piezo-&allowed_in_frame=0.

[7] Jacques Curie and Pierre Curie. "Development by pressure of polar electricity in hemihedral crystals with inclined faces". In: *Bull. soc. min. de France* 3 (1880), p. 90.

[8] M. G. Lippmann. "On the principle of the conservation of electricity". In: (1881).

[9] Jacques Curie and Pierre Curie. "Contractions and expansions produced by voltages in hemihedral crystals with inclined faces". In: *Comptes Rendus* 93 (1881), pp. 1137–1140.

[10] Shaul Katzir. "Who knew piezoelectricity? Rutherford and Langevin on submarine detection and the invention of sonar". In: *Notes Rec. R. Soc.* (2012), rsnr20110049.

[11] Jiashi Yang. "Piezoelectric transformer structural modeling-A review". In: *IEEE transactions on ultrasonics, ferroelectrics, and frequency control* 54.6 (2007).

[12] Ryszard M. Lec. "Piezoelectric sensors". In: *The Journal of the Acoustical Society of America* 104.3 (1998), pp. 1796–1796.

[13] Seung-Bok Choi and Young-Min Han. *Piezoelectric actuators: control applications of smart materials*. CRC Press, 2016.

[14] Nanomotion. *How it Works*. [Online; accessed 09-February-2017]. 2017. URL: http://www.nanomotion.com/piezo-ceramic-motor-technology/works/.

[15] *Proceedings of SPIE*. Vol. 6172. Smart Structures and Materials 2006: Smart Electronics, MEMS, BioMEMS, and Nanotechnology. 2006.

[16] Gianni Ciofani and Arianna Menciassi. *Piezoelectric nanomaterials for biomedical applications*. Springer, 2012.

[17] J. G. Gualtieri, J. A. Kosinski, and J. Ballato. "Piezoelectric materials for SAW applications". In: *IEEE* (1992). DOI: https://doi-org.libproxy.wlu.ca/10.1109/ULTSYM.1992.275972.

[18] Zhong Lin Wang and Jinhui Song. "Piezoelectric nanogenerators based on zinc oxide nanowire arrays". In: *Science* 312.5771 (2006), pp. 242–246.

[19] Petia Dineva et al. "Piezoelectric Materials". In: *Dynamic Fracture of Piezoelectric Materials: Solution of Time-Harmonic Problems via BIEM*. Cham: Springer International Publishing, 2014, pp. 13–15. ISBN: 978-3-319-03961-9. DOI: 10.1007/978-3-319-03961-9_2. URL: http://dx.doi.org/10.1007/978-3-319-03961-9_2.

[20] Haydn N. G. Wadley. "Characteristics and Processing of Smart Materials". In: *In Virginia Univ, Smart Structures and Materials: Implications for Military Aircraft of New Generation p(SEE N 97-11475 01-23)* 1996 (1996).

[21] Seongcheol Mun et al. "Enhanced electromechanical behavior of cellulose film by zinc oxide nanocoating and its vibration energy harvesting". In: *Acta Materialia* 114 (2016), pp. 1–6. URL: https://doi.org/10.1016/j.actamat.2016.05.021.

[22] Xunqian Yin et al. "Mechanical energy harvesting via a plasticizer-modified electrostrictive polymer". In: *Appl. Phys. Lett.* 108 (2016), p. 042901. URL: https://doi.org/10.1063/1.4939859.

[23] Donald J. Leo. *Engineering analysis of smart material systems*. Wiley, 2007.

[24] D. W. Dye. "The piezo-electric quartz resonator and its equivalent electrical circuit". In: *Proceedings of the Physical Society of London* 38.1 (1925), p. 399. URL: http://stacks.iop.org/1478-7814/38/i=1/a=344.

[25] J. Hermann and C. Bourgeois. *Piezo-electric quartz resonator*. US Patent 4,313,071. 1982. URL: https://www.google.com/patents/US4313071.

[26] Colin S. I. Lai et al. "Piezoelectric quartz crystal detection of benzene vapour using chemically modified cyclodextrins". In: *J. Chem. Soc., Perkin Trans. 2*

(3 1988), pp. 319–324. DOI: 10.1039/P29880000319. URL: http://dx.doi.org/10.1039/P29880000319.

[27] Wei-Xiang Wang et al. "Strong piezoelectricity in nanosized silicon nitride prepared by laser-induced chemical vapor deposition". In: *Appl. Phys. Lett.* 62 (1993), p. 321.

[28] C. L. Bowes et al. "Electrical sieves for molecule recognition". In: *Springer Netherlands* (1998), pp. 39–58.

[29] R. Tao et al. "Modeling of semiconducting piezoelectric nanowires for mechanical energy harvesting and mechanical sensing". In: *Nano Energy* 14 (2015), pp. 62–76.

[30] Rodolfo Araneo et al. "Impact of non-linear piezoelectricity on the piezotronic effect of ZnO nanowires". In: *IEEE Transactions on Nanotechnology* 15.3 (2016), pp. 512–520.

[31] Rodolfo Araneo et al. "Current–voltage characteristics of ZnO nanowires under uniaxial loading". In: *IEEE Transactions on Nanotechnology* 13.4 (2014), pp. 724–735.

[32] Zhiming M. Wang. *One-dimensional nanostructures*. Springer, 2008.

[33] Zhai Tianyou and Jiannian Yao. *One-dimensional nanostructures: principles and applications*. Wiley, 2013.

[34] Wenzhuo Wu. "High-performance piezoelectric nanogenerator for self-powered nanosystems: quantitative standards and figures of merit". In: *Nanotechnology* 27.11 (2016), p. 112503.

[35] Geon-Tae Hwang et al. "Self-powered cardiac pacemaker enabled by flexible single crystalline PMN-PT piezoelectric energy harvester". In: *Advanced materials* 26.28 (2014), pp. 4880–4887.

[36] Yan Zhang, Ying Liu, and Zhong Lin Wang. "Fundamental theory of piezotronics". In: *Advanced Materials* 23.27 (2011), pp. 3004–3013.

[37] H. Y. S. Al-Zahrani, J. Pal, and M. A. Migliorato. "Non-linear piezoelectricity in wurtzite ZnO semiconductors". In: *Nano Energy* 2.6 (2013), pp. 1214–1217.

[38] M. A. Migliorato et al. "A review of non linear piezoelectricity in semiconductors". In: *AIP Conf. Proc.* 1590 (2014), pp. 32–41.

[39] Rodolfo Araneo and Christian Falconi. "Lateral bending of tapered piezosemiconductive nanostructures for ultra-sensitive mechanical force to voltage conversion". In: *Nanotechnology* 24.26 (2013), p. 265707.

[40] Rodolfo Araneo et al. "Thermal-electric model for piezoelectric ZnO nanowires". In: *Nanotechnology* 26.26 (2015), p. 265402.

[41] Jiashi Yang. *An introduction to the theory of piezoelectricity*. Vol. 9. Springer Science & Business Media, 2004.

[42] C. Rosen, Basavaraj V. Hiremath, and Robert Newnham. *Piezoelectricity*. 5. Springer Science & Business Media, 1992.

[43] Antonio Rinaldi et al. "Mechanics of quasi-1D ZnO nanostructures for energy harvesting". In: *MRS Online Proc. Library* 1556 (2013). URL: https://doi.org/10.1557/opl.2013.781.

[44] Kory Jenkins et al. "Piezotronic effect: an emerging mechanism for sensing applications". In: *Sensors* 15 (2015), pp. 22914–22940.

[45] Ü. Özgür et al. "A comprehensive review of ZnO materials and devices". In: *Journal of applied physics* 98.4 (2005), p. 11.

[46] Magnus Willander. *Zinc oxide nanostructures: advances and applications*. CRC Press, 2014.

[47] Saurav Siva Kumar et al. "Synthesis, characterization and optical properties of zinc oxide nanoparticles". In: *International Nano Letters* 3 (2013), p. 30.

[48] Y. S. Puzyrev et al. "Memristive devices from ZnO nanowire bundles and meshes". In: *Appl. Phys. Lett.* 111 (2017), p. 153504.

[49] C. A. Ataide et al. "Fast and accurate approximate quasiparticle band structure calculations of ZnO, CdO, and MgO polymorphs". In: *Physical Review B* 95 (2017), p. 045126.

[50] H. Dixit et al. "Accurat pseudopotential description of the GW bandstructure of ZnO". In: *Computer Physics Communications* 182 (2011), pp. 2029–2031.

[51] Zhong Lin Wang. "Toward self-powered sensor networks". In: *Nano Today* 5.6 (2010), pp. 512–514.

[52] Siegfried Selberherr. *Analysis and simulation of semiconductor devices*. Springer, 1984.

[53] Simon M. Sze and Kwok K. Ng. *Physics of semiconductor devices*. Wiley, 2006.

[54] Michael Shur. *Physics of semiconductor devices*. Prentice Hall, 1990.

[55] Charles Kittle. *Introduction to solid state physics*. Wiley, 2005.

[56] Mehrdad Bahrami-Samani, Sunil R. Patil, and Roderick Melnik. "Higher-order nonlinear electromechanical effects in wurtzite GaN/AlN quantum dots". In: *J. Phys.: Condens. Matter* 22 (2010), p. 495301.

[57] Jitendra N. Tiwari, Rajanish N. Tiwari, and Kwang S. Kim. "Zero-dimensional, one-dimensional, two-dimensional and three-dimensional nanostructured materials for advanced electrochemical energy devices". In: *Progress in Materials Science* 57 (2012), pp. 724–803.

[58] Robin D. Lamboll and Neil C. Greenham. "Reduced dimensionality in drift-diffusion models of back-contact solar cells and scanning photocurrent microscopy". In: *Journal of Applied Physics* 122 (2017), p. 133106.

[59] Olgen Penzin et al. "Kinetic velocity model to account for ballistic effects in the drift-diffusion transport approach". In: *IEEE Transactions on Electron Devices* 64.11 (2017), pp. 4599–4606.

[60] Patricio Farrell, Thomas Koprucki, and Jürgen Fuhrmann. "Computational and analytical comparison of flux discretizations for the semiconductor device equations beyond Boltzmann statistics". In: *Journal of Computational Physics* 346 (2017), pp. 497–513.

[61] Yuan He et al. "On the modelling and simulation of reaction-transfr dynamics in semiconductor-electrolyte solar cells". In: *SIAM J. Appl. Math.* 75.6 (2015), pp. 2515–2539.

[62] Timothy Sauer. *Numerical analysis*. Pearson, 2006.

[63] A. Jüngel, R. Pinnau, and E. Röhrig. "Existence analysis for a simplified transient energy-transport model for semiconductors". In: *Math. Meth. Appl. Sci* 36 (2013), pp. 1701–1712.

[64] A. Jüngel. *Quasi-hydrodynamic semiconductor equations*. Springer, 2011.

[65] Martin Vohralik. "On the discrete Poincaré-Friedrichs inequalities for nonconforming approximattions of the Sobolev Space H^1". In: *Numerical Functional Analysis and Optimization* 26.7-8 (2005), pp. 925–952.

[66] Richard Bellman. "The stability of solutions of linear differential equations". In: *Duke Math. J.* 10.4 (1943), pp. 643–647.

[67] B. M. Kayes, H. A. Atwater, and N. S. Lewis. "Comparison of the device physics principles of planar and radial p-n junction nanorod solar cells". In: *Journal of Applied Physics* 97 (2005), p. 114302.

[68] A. Deinega and S. John. "Finite difference discretization of semiconductor equations for naowire solar cells". In: *Computer Physics Communications* 183 (2012), pp. 2128–2135.

[69] D. Vasileska and S. M. Goodnick. *Computational electronics*. Morgan & Claypool Publishers, 2006.

[70] D. L. Scharfetter and H. K. Gummel. "Large-signal analysis of a silicon read diode oscillator". In: *IEEE Trans. Electron Devices* ED-16 (1969), pp. 64–77.

[71] Siegfried Selberherr, Hannes Stippel, and Ernst Strasser. "Simulation of semiconductor devices and processes". In: *Springer* 5 (1993), pp. 237–240.

[72] J. J. H. Miller and Song Wang. "An analysis of the Scharfetter-Gummel box method for the stationary semiconductor device equation". In: *Modélisation mathématique et analyse numérique* 28.2 (1994), pp. 123–140.

[73] Marianne Bessemoulin-Chatard and Claire Chainais-Hillairet. "Exponential decay of a finite volume scheme to the thermal equilibruim for drift-diffusion systems". In: *J. Numer. Math.* 25.3 (2017), pp. 147–168.

[74] Chuanjun Chen and Xiaohan Long. "Finite volume element approximation and analysis for a kind of semiconductor device simulation". In: *J. Appl. Math. Comput.* 33 (2010), pp. 155–172.

[75] COMSOL Inc. "COMSOL Multiphysics Reference Manual". In: *www.comsol.com* 5.1 (2015), p. 980.

[76] Kambiz Salari and Patrick Knupp. "Code verification by the method of manufactured solutions". In: *SANDIA Report* SAND2000-1444 (2000).

[77] William L. Oberkampf and Christopher J. Roy. *Verification and validation in scientific computing*. Cambridge University Press, 2010.

[78] Sia Bhowmick, Roderick Melnik, and Manuele Santoprete. "Nonlinear Coupled Effects in Nanomaterials and their Application for Energy Harvesting". In: *The IV International AMMCS Interdisciplinary Conference* (2017), p. 197.

[79] Fridtjov Irgens. *Continuum Mechanics*. Springer, 2008.

[80] Ya Yang et al. "Pyroelectric nanogenerators for harvesting thermoelectric energy". In: *Nano Lett.* 12.6 (2012), pp. 2833–2838.

[81] R. V. N. Melnik and K. N. Zotsenko. "Mixed electroelastic waves and CFL stability conditions in computational piezoelectricity". In: *Applied Numerical Mathematics* 48 (2004), pp. 41–62.